



HAL
open science

Diagenetic history and porosity evolution of an Early Miocene carbonate buildup (Upper Burman Limestone), Yadana gas field, offshore Myanmar

Thomas Teillet, François Fournier, Franck Gisquet, Lucien F. Montaggioni, Jean Borgomano, Quentin Villeneuve, Fei Hong

► To cite this version:

Thomas Teillet, François Fournier, Franck Gisquet, Lucien F. Montaggioni, Jean Borgomano, et al.. Diagenetic history and porosity evolution of an Early Miocene carbonate buildup (Upper Burman Limestone), Yadana gas field, offshore Myanmar. *Marine and Petroleum Geology*, 2019, 109, pp.589-606. 10.1016/j.marpetgeo.2019.06.044 . hal-02466210

HAL Id: hal-02466210

<https://hal.science/hal-02466210>

Submitted on 25 Oct 2021

HAL is a multi-disciplinary open access archive for the deposit and dissemination of scientific research documents, whether they are published or not. The documents may come from teaching and research institutions in France or abroad, or from public or private research centers.

L'archive ouverte pluridisciplinaire **HAL**, est destinée au dépôt et à la diffusion de documents scientifiques de niveau recherche, publiés ou non, émanant des établissements d'enseignement et de recherche français ou étrangers, des laboratoires publics ou privés.



Distributed under a Creative Commons Attribution - NonCommercial 4.0 International License

Diagenetic history and porosity evolution of an Early Miocene carbonate buildup (Upper Burman Limestone), Yadana gas field, offshore Myanmar

Thomas Teillet ^{1,2}, François Fournier ¹, Franck Gisquet ²,
Lucien F. Montaggioni¹, Jean Borgomano ¹, Quentin Villeneuve ¹, Fei Hong ²

¹ : Aix-Marseille Université, CNRS, IRD, CEREGE, UM 34, 3 Place Victor Hugo, case 67,
13331 Marseille Cedex 03, France

²: TOTAL, CSTJF, Avenue Larribau, 64018 Pau Cedex, France

Abstract

The Miocene Yadana carbonate platform is a major offshore gas reservoir located in the Andaman Sea (offshore Myanmar). The integration of petrographic analysis of carbonate rocks, stable isotope measurements and seismic interpretation provided new insights into the diagenetic history of the Upper Burman Limestone reservoir. The high (28%) average porosity of the reservoir is dominantly related to strong development of microporosity, moldic and vuggy porosity. Mud-supported, coral-rich sediments record significant early marine dissolution of aragonite and early lithification of matrix that has led to the development of dense layers. Stable isotope and petrographic data from the top of the reservoir suggest that the long-term depositional hiatus (middle to late Miocene) was related to platform drowning and non-deposition in a deep marine setting. Moderate dolomitization has affected the top and flanks of the platform during the depositional hiatus. Microporosity development and sparry calcite cementation mainly occurred in marine to marine shallow burial environments. A major decrease in porosity, averaging 10%, below the gas-water contact suggests a major

phase of porosity evolution during and/or after the hydrocarbon emplacement which is mainly
28 related to 1) increased moldic and vuggy porosity development within the gas zone, 2)
microporosity preservation in loosely-packed, subrounded micrites within the gas zone, and
30 3) microporosity reduction by calcite precipitation within the water zone leading to the
development of densely-packed, euhedral micrites.

32

Key words: carbonates, diagenesis, porosity, microporosity, micrite, Miocene, gas reservoir

34

1. Introduction

36

38 The diagenetic evolution of Cenozoic carbonate buildups, from the humid equatorial tropics
of SE Asia, has been widely documented, in particular because these form the reservoirs of
40 many hydrocarbon fields in the region (e.g. Fournier et al., 2004; Sattler et al., 2004; Wilson
and Hall, 2010; Zampetti, 2010). The diagenetic history of such shallow-water carbonate
42 systems is commonly driven strongly by the occurrence of intraformational subaerial
exposure events that have severely modified the mineralogical patterns as well as the volume
44 and structure of the pore networks (e.g. Sun and Esteban, 1994; Saller and Vijaya, 2002;
Sattler et al., 2004; Fournier and Borgomano, 2007; Madden and Wilson, 2013) . In such a
46 context, best reservoirs commonly developed beneath subaerial unconformities in highstand
carbonate buildups that have been subject to intense meteoric water leaching and
48 karstification (Sun and Esteban, 1994; Moldovanyi et al., 1995; Vahrenkamp et al., 2004).
Additionally, the later diagenetic evolution and the reservoir architecture of such shallow-
50 water carbonates have been shown to be largely controlled by porosity and permeability
distribution inherited from early stages of subaerial exposures (Fournier and Borgomano,

52 2007). In a few case studies such as the Miocene carbonates from the Liuhua oil field,
offshore R.P. China (Sattler et al., 2004) and Miocene carbonate buildups from the Luconia
54 Province (Zampetti, 2010), burial dissolution of carbonates has been proposed as a major
process of porosity enhancement.

56 The Lower Miocene Yadana carbonate buildup (Upper Burman Limestone, offshore
Myanmar) is known to be highly porous (av. porosity: 28%) and to be the main reservoir of a
58 significant gas accumulation (Racey and Ridd, 2015). Based on the integration of detailed
petrographic analyses of cores, thin-sections and SEM images, stable isotope (C and O)
60 measurements, well-logs and seismic interpretations, the present paper aims at: (1)
reconstructing the diagenetic history and the porosity evolution of the Lower Miocene Yadana
62 carbonate buildup, (2) identifying the main diagenetic processes that has controlled the
development of a highly porous reservoir in carbonates with little meteoric diagenetic
64 overprint, (3) constraining the timing and processes of evolution and preservation of micrite
microfabrics and associated microporosity and (4) assessing the impact of gas emplacement
66 on the late diagenetic evolution of the reservoir and on the porosity distribution within the
carbonate buildup.

68

70 **2. Geological setting**

The structural framework and the marine and landmass geomorphology of the Andaman Sea
72 area has been strongly controlled by the complex tectonic evolution of SE Asia during the
Cenozoic (Lee and Lawver, 1995; Hall, 2002). During the Paleogene, the northeastward
74 oblique subduction (Sunda subduction zone) of the Indian Plate beneath the Eurasian Plate
(Fig. 1A) resulted in the opening of the Andaman Sea as a back-arc basin (Chakraborty and
76 Khan, 2009; Curray, 2005). In addition, such an oblique subduction led to: 1) major dextral

strike-slip movements along the Sagaing-Andaman-Sumatran fault system, 2) the formation
78 of the Burma microplate, and 3) rifting and spreading of the Andaman Sea within the back-arc
basin (Chakraborty and Khan, 2009; Morley, 2012). During the Oligocene and early Miocene,
80 the Yadana carbonate platform developed on the top of a volcanic ridge east of the Sunda
subduction zone and between the M5 Basin and the Moattama Basin (Morley, 2013; Racey
82 and Ridd, 2015) (Fig. 1C).

84 The Moattama Basin contains Eocene to modern sediments. The lowermost deposits consist
of Upper Eocene volcano-clastics sediments (Fig. 1E). The overlying Oligo-Miocene
86 shallow-water carbonates may reach up to 700 m in thickness, and are subdivided into two
distinct formations (Paumard et al., 2017). These are: (1) the Lower Burman Limestone
88 Formation, late Oligocene in age, that is composed of two distinct carbonate platforms
separated by a central incised valley filled by the Sein clastic formation and (2) the Upper
90 Burman Limestone Formation, early Miocene in age, that is made up of one single carbonate
platform, the top of which corresponds to the gas reservoir of the Yadana Field (Fig. 1D). A
92 long-duration depositional hiatus (~10 Myr) is recorded at top of the Upper Burman
Limestones which are sealed by Upper Miocene (N17, planktonic zone) pro-delta shales
94 (Pyawbwe and Badamayar formations) from the Irrawaddy deltaic system. A major phase of
eastward tilting of the Yadana platform, evidenced by seismic profiles (Fig. 1D), occurred
96 during the Late Miocene (horizon M6: 8.2 Ma, after Paumard et al., 2017). From the Pliocene
to Pleistocene, the Moattama Basin became a major depocentre, with up to 10 km-thick
98 terrigenous deposits supplied from the Irrawaddy deltaic system.

100 **3. Datasets and methods**

102 The present work is based on the analysis of a subsurface database including well logs and
cores. The Upper Burman Limestone has been penetrated by 20 wells. Four wells (WELL-1,
104 WELL-2, WELL-3 and WELL-4) have been selected for the present study (location in Fig.
1B). A total of 343 m of cored sections are available through the reservoir (WELL-1: 87.5
106 mCD (meter Core Depth), WELL-2: 84 mCD WELL-3: 59.5 mCD WELL-4: 112 mCD).
These were described in terms of lithology, depositional features (texture, biological
108 associations) and diagenetic features. A total of 694 thin sections have been prepared from
cores (average spacing of 50 cm). The thin-sections were impregnated with a blue-dye epoxy
110 resin and half-stained with alizarine-red and potassium ferrocyanide solution (Dickson, 1966)
for the identification of carbonate minerals. Thin-sections were observed under polarized-light
112 microscopy for the characterization of depositional and diagenetic features as well as for the
quantitative analysis of pore types. Macroporosity is defined as the pore space which is
114 colored with blue-epoxy and whose size exceeds 2 pixels (i.e. diameter > 10 μm) on scanned
thin-sections. The proportion of macroporosity on thin section is automatically extracted
116 using the software ImageJ by gathering the blue pixels. Microporosity is defined as pores
non-visible on thin section pictures or whose size is lower than 2 pixels (i.e. pore diameter <
118 10 μm). The definition of microporosity used in the present work is therefore consistent with
the definition given by Cantrell and Hagerty (1999). The proportion of microporosity was
120 semi-quantitatively estimated as the difference between the laboratory porosity measured on
plugs and the macroporosity computed from thin-section image analysis. Although based on
122 two-dimensional images, image analysis has been shown to provide accurate quantifications
of macroporosity in carbonate reservoirs (Haines et al., 2015). Petrographic analysis of thin-
124 sections was supported by observations of selected samples of cements under
cathodoluminescence using a 8200 MKII Technosyn (20 kV and 600 mA; Technosyn,
126 Cambridge, UK) coupled to an Olympus microscope (Olympus Optical Corporation, Tokyo,

Japan) and a digital MRc5 camera (Zeiss, Gottingen, Germany). Micrite microfabrics were
128 characterized from environmental scanning electron microscopy (SEM) images performed at
Aix-Marseille University by using a Philips XL30 ESEM ®. Laboratory porosity
130 measurements have been performed on approximately 1000 core-plugs. Vertical changes of
porosity in cored and non-cored intervals have been also investigated by means of well-log
132 data: a porosity log has been computed from density and neutron logs and corrected from gas
effect. Additionally, up to 1000 carbon and oxygen isotope ratios were measured at Erlangen
134 University on bulk samples and selected carbonate components. Carbonate powders were
prepared using a manual micro-drill and reacted with 100% phosphoric acid at 70°C using a
136 Gasbench II connected to a ThermoFisher Delta V Plus mass spectrometer. All values are
reported in per mil relative to V-PDB. Reproducibility and accuracy were monitored by
138 replicate analysis of laboratory standards calibrated by assigning $\delta^{13}\text{C}$ values of +1.95‰ to
NBS19 and -47.3‰ to IAEA-CO9 and $\delta^{18}\text{O}$ values of -2.20‰ to NBS19 and -23.2‰ to
140 NBS18. Reproducibility for $\delta^{13}\text{C}$ and $\delta^{18}\text{O}$ was $\pm 0.06\%$. Elemental determinations of major
(Al, Ca, Mg, Na, K, Ti, Fe, Mn, P, S in percent) and minor elements (including Cu, Pb, Zn,
142 As, U, Th, Sr, Ba in ppm) on whole rock and selected carbonate components (bioclasts,
matrix and cements) were carried out at Bureau Veritas Commodities Canada Ltd.,
144 Vancouver, Canada on total of 17 rock samples, by using inductively coupled plasma
spectrometry (ICP-ES/MS), with a PerkinElmer ICP-MS ELAN® 9000 (PerkinElmer, Inc.,
146 Waltham, Massachusetts, USA) which was calibrated using Bureau Veritas interlaboratory
standards DS10 and Oreas 45Ea. Samples (~1 gram) were pulverized to a fine powder (~3.75
148 phi) and were digested by using the AQ250 Ultra Trace Geochemical aqua regia (HNO₃-HCl)
package for two hours at 95°C. Detection limits range from 1 to 5 ppm for minor elements
150 and averages 0.01% for major elements.

152 4. Results

154 4.1. *Depositional lithofacies of the Upper Burman Limestone*

156 The cored interval from the Upper Burman Limestones is characterized by a relatively
monotonous, 100 m-thick succession of bioclastic limestones (Fig. 2). Skeletal grains are
158 dominated by non-geniculate coralline algae and large benthic foraminifers (Fig. 3A, B, C).
Corals may be common in a few intervals (Fig. 3D). Non-geniculate coralline red algae are
160 dominated by encrusting to branching forms, commonly forming nodules (rhodoliths) (Fig.
3A). The dominant genera are *Lithothamnion*, *Mesophyllum* and *Sporolithon*. Larger benthic
162 foraminiferal association is characterized by *Lepidocyclinids*, *Spiroclypeus*, *Cycloclypeus*
commonly displaying flat-shaped morphologies (Fig. 3C). Scleractinian assemblage includes
164 robust branching or massive forms. Subordinate components include echninoderms,
bryozoans, green algae and rare planktic foraminifera.

166 On the basis of textural and biological features, lithofacies have been identified (Table 1):
coralline algal and foraminiferal floatstone (LF1: Fig. 3A), large benthic foraminiferal
168 grainstone/rudstone (LF2.1: Fig. 3B) and floatstone (LF2.2: Fig. 3C), scleractinian-
echinodermal floatstone (LF3.1: Fig. 3D) and echinodermal wackestone (LF3.2).

170

172 4.2. *Petrography of diagenetic features*

174 The main diagenetic processes observed in cores are dissolution, cementation and
dolomitization. Compaction is relatively weak with rare presence of stylolites in cemented
176 intervals and open fractures.

(1) Carbonate cements

178 Two distinct carbonate cements have been evidenced from petrographic analysis of thin sections: Isopacheous calcite cement (C1) and blocky calcite cement (C2).

180 Isopacheous calcite cement (C1) consists of isopacheous rims of scalenohedral, sparry, nonferroan (stained pink with Alizarin Red S and potassium ferricyanide) calcite crystals, dull
182 brown under cathodoluminescence, averaging 10 μm in thickness (Fig. 4A, B, C). C1 cements may rim large intergranular pores in rudstones or moldic pores after dissolved aragonite
184 bioclasts.

Blocky calcite cements (C2) consist of sparry, nonferroan calcite (50 to 250 μm) occluding
186 intragranular pores in grainstone and rudstones (in gas and water zones), moldic/vuggy pores and fractures (mainly within the water zone) (Fig. 4A, C). Calcite cements C2 have been
188 observed overlying calcite cement rims C1 (Fig.4 A, B, C). These cements are zoned and composed of (Fig. 4B): (1) a first fringe of non-luminescent to dull calcite lining pore wall,
190 (2) a fine and concentric dull to bright orange bands, and (3) a large internal zone occluding the pore and filled by a non-luminescent calcite.

192 Large syntaxial sparry calcite cements (up to few hundreds microns) may also develop around echinoderm pieces in grainstone facies (Fig. 4C).

194

(2) Neomorphic features

196 Calcitized aragonitic bioclasts (dominantly coral fragments) display two types of neomorphic features:

198 1) Calcitized corals dominantly composed of equant calcite crystals (20 to 250 μm) (C2') (Fig. 4D).

200 2) Calcitized corals composed of large (250-1000 μm), orange-brown under natural light,
sparry calcite crystals (CX) (Fig. 4E, F). CX calcites are non-luminescent and have
202 been encountered only within brecciated scleractinian-rich limestones (LF3
lithofacies).

204

(3) *Micrite microfabrics*

206

Four main micrite microfabrics have been identified under SEM in both micritized bioclasts
208 and micrite matrix (Fig. 5).

In the gas zone, high porosity limestones (20-45%) exhibit dominantly loosely-packed,
210 anhedral, subrounded calcimicrites (M1 microfabric: Fig. 5A, B). Subhedral micrite particles
may be present in smaller proportions within the M1 micrite (Fig. 5A). Such micrite may
212 contain interparticle micropores that are larger than the average size of the micrite particles
(around 1 μm), with pore diameters ranging typically from 2 to 10 μm (=micro-vugs: Fig. 5A).

214 Micrite M1 commonly display aggregates (5-10 μm) of coalescent micrite particles (Fig. 5B).

In a few intervals, M1 calcimicrites may coexist in samples with euhedral dolomicrite crystals
216 (M4 microfabric: Fig. 5 B). In gas-bearing limestones with porosity < 20%, both micrite
matrix and micritized allochems exhibit densely packed, coalescent, anhedral micrite crystals
218 (M2 microfabric: Fig. 5C). The M2 micrite microfabric occurs typically in the matrix of
coral-rich floatstones (lithofacies LF3)

220 In the water zone, carbonates display low to moderate microporosity. In both matrix and
micritized bioclasts, micrite crystals are mainly euhedral (M3 microfabric: Fig. 5 D, E) and
222 are coarser (typically 2-4 μ) than gas-zone calcimicrites M1 and M2. Additionally, euhedral
crystals may encase smaller, rounded micrite particles (Fig. 5E).

224 Finally, euhedral dolomicrite particles (from 0.5 to 4 μm) occur within micritized bioclasts
(typically coralline algae) and matrix (Fig. 5 F) from the water and gas legs.

226

(4) *Dissolution features*

228 Selective dissolution of aragonitic skeletal elements (mainly sclereactinians) and subsequent
infill of the moldic pores by sediment (micrite mud and fine-grained skeletal fragments) are
230 common diagenetic features in coral-rich lithofacies (LF3) (Fig. 6 A, B). The sediment
replacing the dissolved septae is of similar nature and in physical continuity with the lime
232 mudstone matrix in which the coral fragment are embedded, thus leading to a faint-ghost
fabric (*sensu* Sanders, 2003)

234 Non-selective dissolution features affecting both aragonitic and calcitic bioclasts as well as
micrite matrix may lead to the formation of moldic pores and vugs (Fig. 7 A), which are
236 devoid of any sediment or cement infill. Such dissolution features contribute significantly to
the porosity of the reservoir (typically 5-20% of the rock volume) within the gas zone but are
238 rarer or absent within the water zone.

240 (5) *Brecciation features*

Brecciated intervals are common within coral floatstones (LF3.1) and echinodermal
242 wackestones (LF3.2) lithofacies. Two distinct carbonate breccias have been identified:

1) Type I breccia: thin beds (<20 cm) of low porosity (<20%) breccia, characterized by
244 poorly sorted, irregular-shaped elements which are commonly interlocked and display
very low displacement (Fig. 6C, 7C). Micrite within the fragments is tight, (M2
246 microfabrics) and the space between fragments is filled with finely bioclastic

wackestone material. The outlines of the clasts commonly display deep embayments
248 (Fig. 6C).

- 2) Type II breccia: thick interval (up to 10 m) of highly porous, loose breccia with large
250 (up to 10cm) angular and poorly sorted fragments which are composed of coral
floatstones. In breccia type II, coral fragments are replaced by CX brownish calcite
252 (Fig. 4F). The space between clasts may be partially filled with a finely bioclastic,
matrix-supported sediment, but residual pore space may be preserved or filled by C2
254 sparry calcite cements.

(6) Dolomitization

256 In various intervals, intragranular and matrix micrite is partially replaced by euhedral
dolomite micro-rhombs (<50 μm) (Fig. 7 B). As revealed by SEM observations (Fig. 5 F),
258 dolomicrite rhombs (M4 microfabric) are associated with M1 calcimicrites. Such dolomitized
intervals do not clearly follow the stratigraphic architecture of the platform: they are common
260 and scattered in some wells (e.g. WELL-2) and almost lacking laterally, in time-equivalent
intervals (e.g. in WELL-1).

(7) Stylolites

264 Compaction features are relatively scarce within the Upper Burman Limestone. In a few thin-
sections, stylolites are overprinted by dissolution vugs (Fig. 7 E).

4.3 Definition of diagenetic facies

268 Diagenetic facies have been defined from the combination of selected petrographic, and
petrophysical parameters (Table 2): 1) diagenetic features, 2) micrite microfabrics, 3) range of
270 porosity values, and 4) pore type association. The significant decrease in average porosity

below the gas-water contact (Fig. 8) and the distinct diagenetic features between the gas-
272 bearing and the water-bearing reservoir led to differentiate the 2 zones in the facies
classification. In the gas zone, in intervals where water saturation is lower than 50, porosity
274 averages 28% (Fig. 8A, B), whereas at higher water-saturation and particularly below the gas-
water contact, porosity decreases significantly (average porosity: 18%) over a 30 meter-thick
276 interval (Fig. 8B)

Within the gas zone, four main groups of diagenetic facies have been identified: 1) highly
278 microporous and vuggy, mud-supported carbonates (G-DF1), 2) microporous cemented
grainstones-rudstones (G-DF2), 3) microporous and vuggy carbonate breccia (G-DF3), 4)
280 floatstones with low matrix microporosity (G-DF4). This diagenetic facies G-DF1 has been
subdivided into 3 sub-facies: calcitic red algal and foraminiferal floatstones (G-DF1A),
282 calcitic coral floatstones (G-DF1B), and partially dolomitized floatstones (G-DF1C).

Within, the water zone, two diagenetic facies have been recognized in the cored interval: 1)
284 floatstones (W-DF1A) and rudstones (W-DF1B) with low intragranular and matrix
microporosity, and 2) carbonate breccia with low microporosity (W-DF2).

286

4.4 Carbon and oxygen stable isotope signatures of selected carbonate components

288

Measurements of carbon and oxygen isotope ratios have been performed from selected
290 carbonate components including red algae, benthic foraminifers, calcitized corals, cements,
dolomite crystals and micrite matrix (Fig. 9).

292 Calcitized corals C2' ($\delta^{18}\text{O} = -4$ to -0‰ V-PDB; $\delta^{13}\text{C} = -0.5$ to -0.3‰ V-PDB), red algae
($\delta^{18}\text{O} = -0.6$ to -2.2‰ V-PDB; $\delta^{13}\text{C} = -0.4$ to $+0.7\text{‰}$ V-PDB) and micritized large benthic
294 foraminifera ($\delta^{18}\text{O} = -0.7$ to -2.9‰ V-PDB; $\delta^{13}\text{C} = -0.5$ to $+0.1\text{‰}$ V-PDB) display a relatively

narrow range of carbon and oxygen signatures that are consistent with Miocene south-east
296 Asian, shallow-water, marine calcite (Fig. 9A) (Ali, 1995; Madden and Wilson, 2013).
Similar signatures are obtained for microporous micrites M1 ($\delta^{18}\text{O} = -2.2$ to -0.1‰ V-PDB;
298 $\delta^{13}\text{C} = -1.0$ to $+1.0\text{‰}$ V-PDB) and densely packed micrites ($\delta^{18}\text{O} = -2.3$ to -0.7‰ V-PDB;
 $\delta^{13}\text{C} = -0.6$ to $+0.2\text{‰}$ V-PDB), whereas euhedral micrites M3 display slightly more negative
300 $\delta^{18}\text{O}$ values ($\delta^{18}\text{O} = -2.9$ to -2.7‰ V-PDB; $\delta^{13}\text{C} = -0.6$ to -0.4‰ V-PDB) (Fig. 9B).

Isopacheous cement (C1) displays a very narrow range of $\delta^{13}\text{C}$ (from 0.0 to -0.7‰ V-PDB)
302 and $\delta^{18}\text{O}$ values (from -1.4 to -1.7‰ V-PDB) (Fig. 9C). In contrast, blocky calcite cement
(C2) exhibits low variations of $\delta^{13}\text{C}$ (from -0.7 to $+0.1\text{‰}$ V-PDB) for a wide range of $\delta^{18}\text{O}$
304 values (from -5.2 to -1.9‰ V-PDB) (Fig. 9C). Calcitized corals CX are significantly depleted
in both ^{18}O and ^{13}C compared to other carbonate components ($\delta^{18}\text{O}$: -5.2 to -6.8‰ V-PDB;
306 $\delta^{13}\text{C}$: -2.7 to -6.2‰ V-PDB) (Fig. 8C). Finally, dolomite rhombs exhibit highly positive $\delta^{18}\text{O}$
(from $+2.6$ to $+3.1\text{‰}$ V-PDB) and $\delta^{13}\text{C}$ (from $+0.8$ to $+1.0\text{‰}$ V-PDB) values (Fig. 9C).

308

4.4 C and O isotopic signature of bulk samples

310

Measurements of carbon and oxygen isotope ratios have been conducted on bulk rock
312 samples at a sampling increment averaging 0.50m on cores from wells WELL-1, WELL-2,
WELL-3 and WELL-4 (Fig. 9D). Bulk rock $\delta^{18}\text{O}$ and $\delta^{13}\text{C}$ values are controlled by the $\delta^{18}\text{O}$
314 and $\delta^{13}\text{C}$ signatures of the individual carbonate phases constituting the carbonate rock. They
are therefore indicative of the processes that have significantly altered the original isotopic
316 composition of the carbonate sediments. The $\delta^{18}\text{O}$ and $\delta^{13}\text{C}$ domains identified for the
different carbonate components (Fig. 9 A, B, C), together with petrographic analysis of cores

318 and thin-sections, help interpreting the vertical variations of the carbon and oxygen isotope ratios of bulk carbonates in cored intervals (Fig. 8, 10).

320 Within the gas zone, highly microporous, mud-supported limestones (coralline algal/foraminiferal G-DF1A and coral floatstones G-DF1B) and grainstones/rudstones (G-
322 DF2), display $\delta^{13}\text{C}$ values ranging from -1 to +0.5‰ and $\delta^{18}\text{O}$ values ranging from -2.8 to +0‰. Both oxygen and carbon isotope signatures are consistent with those of micritized
324 bioclasts, micrite matrix and sparry calcite cements C1 and C2. In contrast, with the water zone, floatstones and rudstones (W-DF1) are marked by more negative $\delta^{18}\text{O}$ values (below -
326 2‰ V-PDB) (Fig. 9E). Negative $\delta^{18}\text{O}$ values coupled with highly negative $\delta^{13}\text{C}$ (below -1 ‰ V-PDB) correspond to brecciated intervals with calcitized coral (CX) from both gas (G-DF3)
328 and water zones (W-DF2) (Fig. 9D, E). Increasing bulk $\delta^{18}\text{O}$ values toward significantly positive values (>+1‰PDB) coupled with moderately positive $\delta^{13}\text{C}$ (0 to +1‰ V-PDB)
330 characterize intervals with significant dolomite content in bulk rock (G-DF1C) (Fig. 9D).

332

4.5 Major and trace elements

334 The concentration values for a selection of major and trace elements have been measured on bioclasts (calcitized corals, large benthic foraminifers and red algae), micrite matrix and
336 cements as well as on bulk rock samples (Table 3). Strontium concentrations in micritized bioclasts (large benthic foraminifers and red algae) range from 407 to 551 ppm. Such values
338 are significantly depleted compared to values known in modern high-Mg calcite skeletal grains (typically higher than 1000 ppm) according to Veizer (1983). Such low values are
340 likely consistent with Sr loss during high-Mg to low-Mg calcite transformation (Veizer, 1983). Strontium concentration in the blocky calcite cement C2 (613 ppm) is significantly

342 lower than those expected in marine low-magnesium calcite (~1000 ppm). Corals
neomorphised into calcite (CX) display the highest Sr concentrations with values of 644 and
344 2019 ppm. Manganese concentrations are generally low within micritized bioclasts (from 18
to 128 ppm), C2 (17 ppm) and CX (11 ppm) calcites. The iron concentrations in all of the
346 measured samples are low (<0.04%). Magnesium concentrations are highly variable in the
analyzed bioclasts (from 0.8 to 1.94%) and depleted in CX and C2 calcite (0.22 and 0.14%
348 respectively). All of the analyzed samples have relatively high sodium concentrations ranging
from 100 to 2200 ppm.

350

352

354 **5. DISCUSSION**

356 **5.1 Origin of diagenetic features and diagenetic environments**

358 The integration of selected petrographic, petrophysical and geochemical parameters led to the
definition of various diagenetic facies (Table 2, Fig. 10, 11) which are characterized by
360 specific paragenesis.

362 ***Highly microporous and vuggy, mud-supported carbonates from the gas zone (G-DF1)***

Within the gas zone, mud-supported carbonates (foraminiferal, coralline algal and coral
364 floatstones) are characterized by significant proportions of dissolution vugs which have been
shown to post-date stylolites, thus suggesting a late phase of leaching in burial environments.

366 The significant drop in porosity (averaging 10%) below the gas-water contact, which is partly
related to a decrease in moldic pore and vug abundance (Fig. 7A, 7B; Fig. 8; Fig. 11) strongly
368 suggests that such a late stage of calcite dissolution occurred during and/or after gas
emplacement.

370 In G-DF1 carbonates, dominant allochems (micritized coralline algae and large benthic
foraminifers) have low-Mg mineralogy and exhibit highly microporous, subrounded micrite
372 microfabric (M1) which is distinct from primary skeletal microfabrics. The carbon and
oxygen isotopic signature of M1 micrites from micritized coralline algae and large benthic
374 foraminifera are consistent with Miocene, south-east Asian, shallow-water, marine calcite
values (Ali, 1995; Madden & Wilson, 2013), thus suggesting that the calcite from M1
376 micrites formed from marine pore fluids at the sea-bottom or in marine, shallow burial
conditions. The common occurrence of subrounded M1 micrite within the gas reservoir and
378 its lack within the water zone may result from 1) preferential dissolution processes within the
gas-bearing reservoir leading to rounded morphologies (Lambert et al., 2006; Volery et al.,
380 2010; Léonide et al., 2014), or 2) preferential preservation of initially anhedral micrites within
the hydrocarbon-zone (Morad et al., 2016). In G-DF1 reservoirs, the micritic matrix mud
382 displays the same micrite microfabric (M1) and the same range of carbon and oxygen isotope
compositions as coralline algae and large benthic foraminifers (Fig. 9 A), thus suggesting
384 similar diagenetic evolution. Although it has been shown that anhedral and subrounded or
knobby micrites may form early in the marine or shallow-burial environment without the
386 intervention of a dissolution process (Morad et al., 2016; Lucia, 2017), the hypothesis of
rounded micrite development during the late phase of leached that affected the gas zone
388 cannot be ruled out.

Among the highly microporous and vuggy carbonates from the gas zone, coral-rich intervals
390 (G-DF1B diagenetic sub-facies) exhibit distinct diagenetic patterns with regards to the early

evolution of aragonitic components. In such intervals, coral are commonly dissolved and
392 filled by a sediment which is closely similar to and in physical continuity with the matrix
(=fossil ghost), thus forming a faint-ghost fabric (Fig. 6 A, B). Filling biomoulds with marine
394 sediment below a subaerial exposure surface would require the existence of a continuous
karstic porosity along which the sediment could infiltrate. The existence of such pathways is
396 unlikely since in faint-ghost fabrics from Yadana, leached corals are generally sparse within
the matrix, and typically non-touching. In contrast, the physical continuation of the biomould
398 fill into the adjacent matrix or into the intragranular pore fill gives evidence of an early phase
of aragonite dissolution in marine environments (Sanders, 2003).

400

Decameter-thick partially dolomitized intervals of mud-supported carbonates (foraminiferal
402 floatstone LF2.2, echinodermal wackestone LF3.2) have been identified in Yadana wells (G-
DF1C diagenetic facies). By considering the Zachos *et al.* (2001) range for Miocene sea-
404 water $\delta^{18}\text{O}$ (from 0 to -1‰ SMOW), and by using the equation linking the fractionation
factors for dolomite with temperature (Epstein *et al.*, 1953; Irwin *et al.*, 1977), the $\delta^{18}\text{O}$ values
406 of dolomite are consistent with a marine parent water at a temperature ranging from 12°C to
 19°C . Such temperatures are significantly cooler than mean tropical sea surface temperatures
408 ($27\text{-}28.5^{\circ}\text{C}$ in the modern Andaman Sea, after Raju *et al.*, 1981) which strongly suggests that
dolomite formed from relatively deep marine water. The oxygen isotope signature of dolomite
410 from Yadana is quite similar to that of Eocene carbonates from the Enewetak atoll ($+2.1$ to
 $+2.7\text{‰}$ PDB after Saller, 1984) and from most of Cenozoic carbonate islands ($+2$ to $+4\text{‰}$
412 PDB after Budd, 1997; Suzuki *et al.*, 2006) where dolomitization has been interpreted to
result from the circulation of cool, deep sea waters.

414

Microporous cemented grainstones-rudstones from the gas zone (G-DF2)

416

In foraminiferal and coralline algal grainstones-rudstones, the isopachous rims of
418 equigranular calcite (C1) around the bioclasts exhibit $\delta^{18}\text{O}$ and $\delta^{13}\text{C}$ values (Fig. 9C) which
strongly suggest that they form in shallow marine environments (Ali, 1995). The calcite
420 cement C2, that typically occludes entirely the intergranular porosity in grainstones and
rudstones have $\delta^{13}\text{C}$ values which are also consistent with a precipitation from marine water
422 (Ali, 1995), but the significantly negative $\delta^{18}\text{O}$ values (from -1.89 to -5.19‰PDB) would
suggest a formation in shallow-burial conditions. By considering the Zachos *et al.* (2001)
424 range for Miocene sea-water $\delta^{18}\text{O}$ (from 0 to -1‰SMOW), and by using the Anderson and
Arthur (1983) equation, a temperature ranging from 20°C to 43°C has been estimated for C2
426 calcite formation, in the case of marine parent waters. In addition, the strontium concentration
values in C2 (613 ppm) would be consistent with those for calcites precipitated from a
428 shallow burial, deep marine water with a lowered Sr/Ca ratio with regards to surface seawater
(Swart, 2015). Additionally, the extremely low Fe (<0.01%) contents and the relatively
430 elevated Na concentration (100 ppm) in C2 support the interpretation of a non-meteoric origin
for parent fluids, even though the possibility of a contamination by Na from fluid inclusions
432 cannot be discarded.

As for G-DF1 diagenetic facies, G-DF2 limestones are strongly affected by extensive non-
434 selective dissolution features (vugs) cross-cutting stylolites. The lack of calcite cement within
such vugs strongly suggest that dissolution postdates the formation of the early marine to
436 marine shallow burial C2 cements.

438 ***Microporous and vuggy carbonate breccia from the gas zone (G-DF3)***

Highly porous carbonate breccia (G-DF3) form a 5 meter-thick interval with frequent
440 brownish calcitized corals (CX). The negative signature in both $\delta^{13}\text{C}$ (from -2.7 to -6‰ PDB)
and $\delta^{18}\text{O}$ (from -5.2 to -6.8‰ PDB) would be consistent with calcitization processes
442 controlled by meteoric water. By considering meteoric water temperatures ranging from 20 to
30°C, a $\delta^{18}\text{O}$ value of -2.5 to -6‰ V-SMOW has been calculated for the parent fluids by
444 using the Anderson and Arthur (1983) equation. Such a value is consistent with the modern
precipitation $\delta^{18}\text{O}$ values recorded in the Andaman Islands (Laskar et al., 2011: +0.7 to -5.2‰
446 V-SMOW) and in low latitude in SE Asian area (Bowen & Wilkinson, 2002: -4 to -6‰ V-
SMOW). In addition, the meteoric origin of CX calcite is also supported by the elevated
448 strontium concentration (2019 ppm) since aragonite calcitization in meteoric environments
has been shown to retain significant proportions of the original strontium amount, with final
450 concentrations in calcite commonly higher than 2000 ppm, particularly in the vadose zone
(Pingitore, 1976; Webb et al., 2009). Furthermore, the Sr/Ca and Mg/Ca weight ratio for CX
452 calcite are within the range of published values for low-magnesium calcite replacing coral
aragonite and also for interskeletal low-magnesium calcite in calcitized corals (Rabier et al.,
454 2008). Calcite CX exhibits crystal overgrowths developing into the inter-clast space. These
are sealed by finely bioclastic micrite of probable marine origin as suggested by its stable
456 isotope signature (Fig. 9C; $\delta^{18}\text{O}$: -1‰ PDB; $\delta^{13}\text{C}$: +0.2‰ PDB). This suggests that coral
calcitization and CX calcite overgrowth occurred during or after brecciation but prior to
458 marine micrite infill, and are therefore early diagenetic features. These indices strongly
suggest that brecciation processes and calcitization of corals into CX occurred during an
460 early, intraformational, stage of subaerial exposure.

462 *Coral floatstones with low matrix microporosity from the gaz zone (G-DF4)*

The low to moderate porosity values (10-25%) for G-DF4 coral floatstones is related to the
464 low interparticle microporosity within matrix micrite (**M2** microfabrics). As for G-DF1B
diagenetic facies, early marine dissolution of aragonite is evidenced by the occurrence of
466 faint-ghost textures. The carbon and isotope signatures of micrites and bulk carbonates from
such dense G-DF4 intervals (Fig. 9B, D) suggest that M2 micrites formed and became
468 lithified in marine environments. Brecciated limestones (type I breccia) typically occur at top
of G-DF4 intervals (Fig. 7 C, 10, 11). The clasts consist of paraautochthonous fragments of
470 coral floatstone (LF3.1) displaying the densely-packed, anhedral micrite **M2**. They are
embedded within an echinoderm-rich wackstone matrix with **M1** micrite, thus suggesting
472 early lithification and early brecciation of the coral floatstone. This also strongly demonstrates
that the densely-packed, anhedral micrite **M2** results from early lithification processes on the
474 sea-bottom. Tops of these brecciated intervals are commonly bored by lithophagous molluscs
and are sharply overlain by LF1 or LF2.1 facies (Fig. 7 C) thus suggesting hardground
476 surfaces that formed during periods of non-deposition.

478 *Low microporosity carbonates (W-DF1 and W-DF2) from the water zone*

As revealed by laboratory measurements and counting on thin-section, the sharp decrease in
480 porosity below the gas water-contact is mainly related to low intragranular and matrix
microporosity and in a decrease in moldic and vuggy pores (Fig. 8).

482 Carbonates from the water zone display the same early diagenetic features as those evidenced
in the gas zone: 1) micritization and high-Mg to low-Mg calcite conversion of foraminifera
484 and coralline algae, 2) early marine dissolution of aragonite in coral-rich intervals (faint-ghost
texture), 3) brecciation and calcitization of corals into CX below subaerial exposure surface;
486 4) occlusion of intergranular pore by C1 and C2 calcite. SEM observations of micrites from

the water zone revealed a densely-packed euhedral microfabric (M3: Fig. 5C). The occurrence
488 of smaller (~1 μm) and rounded micrite particles which are encased within larger (~2-4 μm)
euhedral crystals may suggest that M3 euhedral micrite results from: 1) the transformation of
490 rounded micrite into euhedral micrite and microspar (aggrading neomorphism), via
precipitation of syntaxial calcite micro-overgrowths around micrite (Morad et al., 2016) or 2)
492 recrystallization involving the dissolution of micrite and reprecipitation of euhedral calcite
(Richard et al., 2007; Volery et al., 2010, Deville de Periere et al., 2011 ; Léonide et al.,
494 2014). In addition, lower $\delta^{18}\text{O}$ values have been measured in micritized benthic foraminifers
from the water zone ($\delta^{18}\text{O} = -2.7$ to -2.9‰) compared to the gas zone ($\delta^{18}\text{O} = -2.0$ to -2.2‰),
496 which likely results from an increase in precipitation temperature in the water zone, assuming
similar oxygen isotopic composition of the porewaters (Dickson and Coleman, 1980). The
498 stable isotope composition of such micrites probably reflects that of a mixture between a
micrite precursor (anhedral micrite?) and calcite micro-overgrowths, thus only minimum
500 temperatures of euhedral micrite formation can be obtained using $\delta^{18}\text{O}$ values on micritized
grains. By considering the Zachos *et al.* (2001) range for Miocene sea-water $\delta^{18}\text{O}$ (from 0 to -
502 1 ‰ SMOW), and by using the Anderson and Arthur (1983) equation, a minimum temperature
ranging from 23°C to 29°C has been estimated for calcite micro-overgrowth formation, in the
504 case of marine parent waters. Higher temperatures (38-41°C) are obtained if precipitation is
assumed to have occurred from evolved marine pore waters ($\delta^{18}\text{O}-\text{SMOW} = +2\text{‰}$ after
506 Egeberg and Aagaard, 1989). The latter values are closer to that of the present-day reservoir
temperature (55°C).

508

5.2 Diagenetic history of the Upper Burman Limestone

510

Petrographic and stable isotopic studies allow the diagenetic history of the Upper Burman
512 Limestone Formation to be reconstructed. The burial curve of the Yadana platform, the
diagenetic model and the tectonic reconstruction of the region proposed in this paper are
514 summarized in Fig. 12.

Step 1: Early Miocene: early marine and shallow-burial marine diagenesis

516 A major feature of early marine diagenesis of the coral-rich limestones (LF3.1 lithofacies),
occurring at the sea-bottom or near the sea-bottom is extensive aragonite dissolution and
518 subsequent marine sediment infills that led to the development of faint-ghost fabrics. Such
early dissolution features have been interpreted as resulting from undersaturation of shallow-
520 marine waters with increased organic matter degradation at the sea-bottom (e.g. Reaves, 1986;
Sanders, 2003). During periods of low sedimentation rates, low porosity M2 micrite
522 microfabrics developed. Such an early lithification of mud matrix favored the early
brecciation of LF3.1 and LF3.2 limestones. In coral-rich (LF3.1) and coralline algal-
524 foraminiferal limestones (LF1 and LF2 lithofacies), the conversion of high-Mg into low-Mg
calcite and the micritisation of bioclasts (red algae and large benthic foraminifers) probably
526 occurred during early marine to shallow-burial, marine diagenesis, as suggested by marine,
low temperature stable isotope signatures (Fig. 9B) of M1 micrites. In grain-supported
528 sediments (LF2.1 lithofacies), minor calcite cementation occurred (C1 sparry calcite cement)
in shallow-marine environments at water temperatures ranging from 18 to 24°C, as calculated
530 from the range of $\delta^{18}\text{O}$ values of C1 calcite and Miocene seawater (0 to -1‰ SMOW, after
Zachos et al., 2001) .

532

Step 1': Early Miocene: intra-formational subaerial exposure

534 The scattered brownish calcitized corals (CX) with distinct meteoric isotope signature, are the
only potential evidence of carbonate precipitated in freshwater in the whole Yadana core
536 dataset. Their occurrence within one correlatable brecciated interval may suggest the
existence of one subaerial exposure event having interrupted the development history of the
538 Yadana carbonate platform. According to Miller *et al.* (2005), the amplitude of eustatic
variations during the Early Miocene may have reached 30 m thus making possible the
540 subaerial exposure during regional sea-level drops of shallow-water carbonates.

542 *Step 2: Middle-Late Miocene: long-duration (~10 Myr) depositional hiatus*

A 10 Myr-long hiatus (Burdigalian to Tortonian) has been evidenced between the top of the
544 Upper Burman Limestone (Early Miocene) and the overlying shales forming the Pyawbwe
Formation (Late Miocene) (see burial curve: Fig. 12). Contemporaneously, a significant
546 depocenter developed to the west, in the M5 Basin resulting in the deposition of 1500 m thick
Middle terrigenous sediments during the Late Miocene. The uppermost Upper Burman
548 carbonates as well as the limestones reworked at the base of the overlying marls do not
present any petrographic or geochemical evidence of meteoric weathering. All of the bulk and
550 micro-sampling isotope measurements performed in the uppermost Upper Burman carbonates
are consistent with early marine or marine shallow burial signatures. In addition, no trend of
552 decreasing $\delta^{13}\text{C}$, that could indicate a subaerial exposure surface at top of Yadana limestone
(Matthews and Allan, 1982), has been evidenced in the cored intervals from the four studied
554 wells (Fig. 8, 10). The more comprehensive interpretation for the long-duration hiatus
occurring at top of Upper Burman limestones is the drowning of the Yadana platform during
556 the Burdigalian which prevented shallow marine sedimentation to occur. Long-term, marine
depositional hiatuses are common features of submerged seamounts from the Pacific where

558 Eocene to Miocene shallow-water carbonates are exposed in deep sea-water at the top of
seamounts (Takayanagi et al., 2012) .

560 Even though microporosity development in Yadana may have started to develop during early
marine diagenesis, high microporosity in calcitic sediments affected by cool seawater has
562 been observed in Pacific atolls (Saller & Moore, 1989). The marine isotopic signature of
dolomite, similarly to that from the Enewetak platform (Saller, 1984; Saller & Moore, 1989)
564 indicates dolomitization of the Yadana carbonates by cool (12-19°C), marine water and
therefore likely occurred presumably prior to significant burial. The occurrence of a
566 dolomitized horizon on top of the reservoir, just below the overlying Pyawbwe Shales may
suggest that dolomitization occurred during the period of non-deposition, in relatively deep-
568 water setting. Similarly, dissolution and dolomitization in deep seawater has been described in
slope sediments from the Bahamas (Mullins et al., 1985).

570

Step 3: Upper Miocene – Present: Cementation, euhedral calcimicrite development (M3)

572 *and late dissolution in burial environment*

During the late Miocene, the opening and the spreading of the Andaman Sea resulted in
574 increased subsidence in the Yadana area (Chakraborty and Khan, 2009; Curray, 2005). After a
10 My-long hiatus, the Yadana platform has become buried below approximately 1000 m-
576 thick latest Miocene to Quaternary terrigenous marine sediments. Based on carbon and
oxygen isotope signatures, the blocky calcite cements C2 that occlude most of the
578 intergranular or intraskeletal porosity in the whole studied interval are regarded as having
precipitated from marine pore water at temperatures ranging from 20 to 43°C. Such
580 temperatures suggest that sparry calcite C2 cementation occurred therefore partially or
entirely during the post-hiatus burial stage (Fig. 12).

582 The widespread development of open vugs is interpreted to have occurred during the burial
stage since these dissolution features overprint calcite C2 cements and stylolites. In addition,
584 the increased abundance in moldic and vuggy porosity in the gas zone strongly suggests that
most of the burial dissolution occurred during and after the gas emplacement. The dominance
586 of highly porous M1 micrites within the gas zone and its scarcity within the water zone may
be related to a differential preservation of early-formed anhedral, subrounded micrites in a
588 reservoir with high hydrocarbon saturation (Morad et al., 2016). However, the hypothesis of
rounded micrite development by dissolution processes (Lambert et al., 2006) cannot be ruled
590 out. Various potential sources for aggressive fluids that have been used to explain burial
porosity creation in carbonates can be identified: 1) carbon dioxide and organic acids from
592 kerogen (Mazzullo & Harris, 1991; Morad et al., 2000), 2) high inorganic CO₂ inputs from
presumed metamorphic or igneous rocks (Beavington-Penney et al., 2008), 3) hydrocarbon
594 biodegradation (Ehrenberg and Jakobsen, 2001), 4) hydrogen sulfide oxidation (Hill, 1990),
5) mixing corrosion (Esteban and Taberner, 2003), 6) thermochemical sulfate reduction
596 (Machel, 2001), and 7) thermal convection (Bjørlykke et al., 1988).

Since late dissolution features are mostly located within the gas-bearing reservoir, water
598 acidification by CO₂ and organic acids resulting from methane biodegradation (Behar and
Albrecht, 1984) can be considered as a potential cause of undersaturation in the Yadana
600 reservoir. CO₂ is present within the gas zone (around 9% of the total gas volume) and may
have contributed to significant carbonate undersaturation in residual water within the gas zone
602 and at the gas migration front. As suggested by Lambert et al. (2006), dissolution could have
occurred during gas emplacement, with organic acids and CO₂ moving downward with the
604 advancing gas-water-contact. In this case, dissolved carbonates may have been transported
downward into the water-zone, together with water moving downward during gas
606 emplacement, and precipitated as calcite micro-overgrowths (M3 micrite) or C2 calcite within

connected macropores. Dissolution may also have occurred after gas emplacement, by
608 acidification of residual water saturation (Lambert et al., 2006), but in that case, a flow of
residual water is needed to transport dissolved calcite (Ehrenberg et al., 2012) and maintain
610 significant dissolution. The lack of preserved or relict sulfates, and sulfides in the Upper
Burman limestone as well as the extreme scarcity of H₂S (<4ppm) in the gas composition do
612 not support the hypothesis of hydrogen sulfide oxidation or thermochemical sulfate
reduction as major processes for secondary porosity development.

614 Finally, the major shift of porosity around the GWC (Fig. 8B) suggests a major phase of
porosity evolution during and/or after the hydrocarbon emplacement which is mainly related
616 to 1) differential moldic and vuggy porosity development within the gas zone, 2)
microporosity preservation or enhancement in M1 micrites within the gas zone, and 3)
618 microporosity reduction by calcite micro-overgrowth leading to densely-packed, euhedral M3
microfabric.

620

5.3 Contrasting patterns of porosity evolution in Oligo-Miocene SE Asian carbonate 622 hydrocarbon reservoirs

Isolated carbonate buildups are common in Cenozoic of SE Asia and are known to be
624 significant hydrocarbon reservoirs : e.g. Liuhua platform (Sattler et al., 2004; Zampetti et al.,
2005), Luconia platform (Epting, 1980; Vahrenkamp, 1998; Sattler et al., 2004), Malampaya
626 platform (Fournier et al., 2004; Fournier and Borgomano, 2007). Such reservoirs are highly
porous with porosity values commonly reaching 40%, and display a high proportion of
628 secondary macropores (molds and vugs) and microporosity. Park et al. (1995) linked the
increase in reservoir quality in the lower Miocene Batu Raja limestones from Indonesia to the
630 repeated subaerial exposure events. Sun and Esteban (1994) emphasized the role of third-

order sea-level drops and subsequent subaerial exposures on the regional development of
632 Miocene carbonate reservoirs from South-East Asia. In addition, the development of elevated
secondary porosity (moldic pores and microporosity) in the Luconia Province has been related
634 to meteoric diagenesis during prolonged phases of subaerial exposure. However, for Zampetti
et al. (2004), in the Luconia platforms, secondary porosity has been interpreted as having
636 dominantly developed in burial environments. In the Liuhua isolated platform, there is little
evidence of intraformational subaerial exposure events and secondary porosity has been
638 shown to be largely related to burial leaching (Sattler et al., 2004). In the Tonasa Platform,
central Indonesia (Eocene to Miocene), diagenetic features related to subaerial exposure are
640 uncommon, mainly localized around faulted highs, formed during the major-mid Oligocene
eustatic fall although deposition occurred mainly close to sea surface on top of the platform
642 (Arosi and Wilson, 2015). The scarcity of exposure related-features outside of faulted highs
has been interpreted as resulting from the combined effect of relatively high subsidence rates
644 and low rates of carbonate production and accumulation in foraminiferal-dominated carbonate
systems (BouDagher-Fadel and Wilson, 2000; Wilson, 2008; Arosi and Wilson, 2015).

646 Similarly, in Yadana, only one subaerial exposure event has been identified in the studied
interval. The poor development of diagenetic features related to subaerial exposition is likely
648 to be due to the low amplitude of eustatic variations during the Early Miocene and/or to high
subsidence rates and in the case of effective emergence, the vadose zone is expected to be
650 extremely reduced in thickness.

In contrast, the Oligo-Miocene Malampaya carbonate buildup (offshore Palawan,
652 Philippines), was affected by cyclic, repeated subaerial exposure events recorded by thick (up
to 5m) pedogenetized intervals (Fournier et al., 2004). However, in spite of such repeated
654 subaerial exposure events, most of the secondary porosity (molds, vugs, microporosity) has

been shown to have mainly developed during burial (Fournier and Borgomano, 2007;
656 Warrlich et al., 2010).

The different Cenozoic South-East Asian carbonates have responded differentially to the
658 development of low porosity intervals. In the Yadana platform, low porosity units within the
gas zone are rare and related to early marine lithification of micrite matrix below
660 hardgrounds. In the Miocene Zhujiang carbonates in the Liuhua field (South-China Sea), tight
intervals are related both to early meteoric phreatic and late burial calcite cementation (Sattler
662 et al., 2004). In the Miocene E11 field from Central Luconia, low porosity intervals results
from increased clay content and early marine and/or meteoric cementation (Warrlich et al.,
664 2010). In the Malampaya field, low porosity units result from the late burial cementation of
previously highly permeable pedogenetized intervals (Fournier & Borgomano, 2007). From
666 the foregoing, it appears clearly that in the different Cenozoic South-East Asian carbonate
reservoirs, early depositional and diagenetic processes have played a key role in the
668 development of low-porosity units.

However, the diagenetic analysis of the Yadana reservoir revealed, for the first time in
670 Cenozoic carbonate reservoirs from SE Asia, a significant porosity reduction below a
hydrocarbon-water contact which resulted from preferential calcite micro-overgrowths in
672 water zone micrites. Such a process of late porosity reduction in carbonate reservoirs probably
exists in other microporous carbonates from South East Asia, but the scarcity of cores in
674 water zones limits its detection.

676 **CONCLUSIONS**

678 Petrographic and stable isotopic analyses allow the diagenetic history of the Upper Burman
Limestone Formation to be reconstructed.

680 1) The high (28%) average porosity of the Yadana gas reservoir is dominantly related to
significant development of microporosity in micritized grains and matrix (loosely-packed,
682 subrounded micrite M1) as well as moldic and vuggy porosity.

2) Mud supported, coral-rich sediments have undergone significant early marine dissolution
684 of aragonite grains (faint-ghost texture) and lithification of micrite matrix (densely-packed
and coalescent anhedral micrite M2), thus leading to the development of dense layers.

686 3) One potential subaerial exposure surface correlatable through wells has been evidenced at
top of a brecciated interval which is characterized by the occurrence of scattered calcitized
688 corals with negative $\delta^{13}\text{C}$ signature (CX calcite). With the exception of this thin (<10m)
interval, the Upper Burman carbonates show no petrographic or geochemical evidence of
690 meteoric overprint.

4) Stable isotope and petrographic data from the top of the UBL suggest that the associated
692 long-term depositional hiatus (Middle to Late Miocene: ~10Myr) was related to platform
drowning and non-deposition in a deep marine setting. Partial dolomitization, which affected
694 preferentially the top and flanks of the platform, likely occurred during such a hiatus, in deep
marine environment.

696 5) Microporosity development and formation of loosely-packed, subrounded micrites (M1
microfabric) likely mainly occurred in marine to marine shallow burial environments.

698 6) The major decrease in porosity (averaging 10%) below the gas-water contact results from a
major phase of porosity evolution during and/or after the gas emplacement. Such a porosity
700 shift is mainly related to 1) increased moldic and vuggy porosity development within the gas
zone, 2) microporosity preservation in loosely-packed, subrounded micrites (M1) within the
702 gas zone, and 3) microporosity reduction by calcite micro-overgrowth within the water zone
leading to the development of densely-packed, euhedral micrites (M3).

704 The present findings provide therefore new insights into the porosity evolution in gas
reservoirs from Cenozoic, South-East Asian carbonate buildups.

706

ACKNOWLEDGMENTS

708

The present study is part of a PhD work (PhD student: Thomas Teillet) funded by
710 TOTAL R&D CARBONATES, Pau, France. TOTAL and partners (CHEVRON, MOGE)
are also greatly acknowledged for the database, the technical support and the clearance
712 for publishing the study. Alain Tonetto (Aix-Marseille University) is greatly thanked for
his support in the acquisition of SEM images. This manuscript has also benefited greatly
714 from the detailed and constructive remarks from Conxita Taberner and from an
anonymous reviewer.

716

REFERENCES

718

Ali, M.Y., 1995. Carbonate cement stratigraphy and timing of diagenesis in a Miocene mixed
720 carbonate–clastic sequence, offshore Sabah, Malaysia—constraints from
cathodoluminescence, geochemistry and isotope studies. *Sediment. Geol.*, 99, 191–214.

722

Anderson, T.A.M., Arthur, M.A., 1983. Stable isotopes of oxygen and carbon and their
724 application to sedimentologic and paleoenvironmental problems, in: Arthur, M.A., Anderson,
T.F., Kaplan, I.R., Veizer, J., and Land, L.S. (Eds.), *Stable Isotopes in Sedimentary Geology*,
726 SEPM, Short Course 10, pp. 1-1–1-151.

728

Arosi, H.A., Wilson, M.E.J., 2015. Diagenesis and fracturing of a large-scale, syntectonic
carbonate platform. *Sediment. Geol.*, 326, 109–134.

730

Beavington-Penney, S.J., Nadin, P., Wright, V.P., Clarke, E., McQuilken, J., Bailey, H.W.,
732 2008. Reservoir quality variation on an Eocene carbonate ramp, El Garia Formation, offshore
Tunisia: Structural control of burial corrosion and dolomitisation. *Sediment. Geol.*, 209, 42–
734 57.

736

Behar, F.H., Albrecht, P., 1984. Correlations between carboxylic acids and hydrocarbons in
several crude oils. Alteration by biodegradation. *Org. Geochem.*, 6, 597–604.

738

- 740 Bjørlykke, K., Mo, A., Palm, E., 1988. Modelling of thermal convection in sedimentary
basins and its relevance to diagenetic reactions. *Mar. Petrol. Geol.*, 5, 338–351.
- 742 BouDagher-Fadel, M.K., Wilson, M., 2000. A revision of some larger foraminifera of the
Miocene of Southeast Kalimantan. *Micropaleontology*, 46, 153–165.
- 744
- 746 Bowen, G.J., Wilkinson, B., 2002. Spatial distribution of $\delta^{18}\text{O}$ in meteoric precipitation.
Geology, 30, 315–318.
- 748 Budd, D.A., 1997. Cenozoic dolomites of carbonate islands: Their attributes and origin, *Earth
Sci. Rev.*, 42, 1-2, 1-47.
- 750
- 752 Cantrell, D.L., Hagerty, R.M., 1999. Microporosity in Arab Formation carbonates, Saudi
Arabia. *GeoArabia*, 4, 129-154.
- 754 Chakraborty, P.P., Khan, P.K., 2009. Cenozoic geodynamic evolution of the Andaman-
Sumatra subduction margin: Current understanding. *Isl. Arc*, 18, 184–200.
- 756
- 758 Curray, J.R., 2005. Tectonics and history of the Andaman Sea region. *Journal of Asian Earth
Science*, 25, 187–232.

- 760 Deville de Periere, M., Durllet, C., Vennin, E., Lambert, L., Bourillot, R., Caline, B., Poli, E.
2011. Morphometry of micrite particles in Cretaceous microporous limestones of the Middle
762 East: influence on reservoir properties. *Mar. Petrol. Geol.*, 28, 1727–1750.
- 764 Dickson, J.A.D., 1966. Carbonate identification and genesis as revealed by staining. *J. Sedim.
Res.*, 36, 2, 491-505.
- 766
- Dickson, J.A.D., Coleman, M.L., 1980, Changes in carbon and oxygen isotopic composition
768 during limestone diagenesis. *Sedimentology*, 27, 107-118.
- 770 Egeberg, P.K., Aagaard, P. 1989. Origin and evolution of formation waters from oil fields on
the Norwegian shelf. *Applied Geochemistry*, 4, 131–142.
- 772
- Ehrenberg, S.N., Jakobsen, K.G., 2001. Plagioclase dissolution related to biodegradation of
774 oil in Brent Group sandstones (Middle Jurassic) of Gullfaks Field, Northern North Sea.
Sedimentology 48, 703–721.
- 776
- Ehrenberg, S.N., Walderhaug, O., Bjørlykke, K., 2012. Carbonate porosity creation by
778 mesogenetic dissolution: reality or illusion? *AAPG Bull.*, 96, 2, 217-233.
- 780 Epstein, S., Buchsbaum, R., Lowenstam, H.A., Urey, H.C., 1953. Revised Carbonate-Water
Isotopic Temperature Scale. *Geol. Soc. Amer. Bull.*, 64, 1315–1325.

782

Epting, M., 1980. Sedimentology of Miocene Carbonate Buildups Central Luconia Offshore

784 Sarawak. Geol. Soc. Malaysia Bull., 12, 17-30.

786 Esteban, M., Taberner, C., 2003. Secondary porosity development during late burial in
carbonate reservoirs as a result of mixing and/or cooling of brines. J. Geoch. Explor., 78–79,

788 355–359.

790 Fournier, F., Borgomano, J., 2007. Geological significance of seismic reflections and imaging
of the reservoir architecture in the Malampaya gas field (Philippines). AAPG Bull., 91, 2,

792 235-258.

794 Fournier, F., Montaggioni, L., Borgomano, J., 2004. Paleoenvironments and high-frequency
cyclicality from Cenozoic South-East Asian shallow-water carbonates: A case study from the

796 Oligo-Miocene buildups of Malampaya (Offshore Palawan, Philippines). Mar. Petrol. Geol.,
21, 1–21.

798

Haines, T.J., Neilson, J.E., Healy, D., Michiea, E.A.H., Aplin, A.C., 2015. The impact of

800 carbonate texture on the quantification of total porosity by image analysis. Computers and
Geosciences., 85, 112-125.

802

Hall, R., 2002. Cenozoic geological and plate tectonic evolution of SE Asia and the SW
804 Pacific: Computer-based reconstructions, model and animations. *J. Asian Earth Sci.*, 20, 353–
431.

806

Hill, C.A., 1990. Sulfuric acid speleogenesis of Carlsbad Cavern and its relationship to
808 hydrocarbons, Delaware Basin, New Mexico and Texas. *AAPG Bull.*, 74, 11, 1685-1694.

810 Irwin, H., Curtis, C., Coleman, M., 1977. Isotopic evidence for source of diagenetic
carbonates formed during burial of organic-rich sediments. *Nature*, 269, 209–213.

812

Lambert, L., Durllet, C., Loreau, J.P., Marnier, G., 2006. Burial dissolution of micrite in
814 Middle East carbonate reservoirs (Jurassic-Cretaceous): Keys for recognition and timing.
Mar. Petrol. Geol., 23, 79–92.

816

Laskar, A.H., Raghav, S., Yadava, M.G., Jani, R.A., Narayana, A.C., Ramesh, R., 2011.
818 Potential of stable Carbon and Oxygen isotope variations of speleothems from Andaman
Islands, India, for paleomonsoon reconstruction. *J. Geol. Res.*, 2011, 1–7.

820

Lee, T.Y., Lawver, L.A., 1995. Cenozoic plate reconstruction of Southeast Asia.
822 *Tectonophysics*, 251, 85–138.

- 824 Léonide, P., Fournier, F., Reijmer, J.J.G., Vonhof, H., Borgomano, J., Dijk, J., Rosenthal, M.,
van Goethem, M., Cochard, J., Meulenaars, K., 2014. Diagenetic patterns and pore space
826 distribution along a platform to outer-shelf transect (Urgonian limestone, Barremian–Aptian,
SE France). *Sediment. Geol.*, 306, 1–23.
- 828
- Lucia, J.F., 2017. Observations on the origin of micrite crystals. *Mar. Petrol. Geol.*, 86, 823-
830 833.
- 832 Machel, H.G., 2001. Bacterial and thermochemical sulfate reduction in diagenetic settings -
old and new insights. *Sediment. Geol.*, 140, 143–175.
- 834
- Madden, R.H.C., Wilson, M.E.J., 2013. Diagenesis of a SE Asian Cenozoic carbonate
836 platform margin and its adjacent basinal deposits. *Sediment. Geol.*, 286–287, 20–38.
- 838 Matthews, R.K., Allan, J.R., 1982. Isotope signature associated with early meteoric
diagenesis. *Sedimentology*, 29, 797–817.
- 840
- Mazzullo, S.J., Harris, P.M., 1991. An overview of dissolution porosity development in the
842 deep-burial environment, with examples from carbonate reservoirs in the Permian Basin.
Permian Basin Play, in: Candelaria, M. (Ed.), *Permian Basin Plays - Tomorrow's Technology*
844 Today: West Texas Geological Society (and Permian Basin Section SEPM) Publication, pp.
125-138.

846

Miller, K.G., Kominz, M.A., Browning, J. V., Wright, J.D., Mountain, G.S., Katz, M.E.,

848 Sugarman, P.J., Cramer, B.S., Christie-Blick, N., Pekar, S.F., 2005. The phanerozoic record
of global sea-level change. *Science*, 310, 1293–1298.

850

Moldovanyi, E.P., Wall, F.M., Yan, Z.J., 1995. Regional exposure events and platform
852 evolution of Zhujiang Formation carbonates, Pearl River mouth basin: evidence from primary
and diagenetic seismic facies, in: Budd, D.A., Saller, A.H. and Harris, P.M. (Eds.),

854 Unconformities and Porosity in Carbonate Strata, AAPG Memoir 63, pp. 125–140.

856 Morad, D., Paganoni, M., Al Harthi, A., Morad, S., Ceriani, A., Mansurbeg, H., Al Suwaidi,
A., Al-Aasm, I.S., Ehrenberg, S.N., 2016. Origin and evolution of microporosity in

858 packstones and grainstones in a Lower Cretaceous carbonate reservoir, United Arab Emirates,
in: Armitage, P. J., Butcher, A. R., Churchill, J. M., Csoma, A. E., Hollis, C., Lander, R. H.,

860 Omma, J. E.,

Worden, R. H. (Eds.), *Reservoir Quality of Clastic and Carbonate Rocks: Analysis, Modelling*

862 and Prediction. Geological Society, London, Special Publications, 435, pp. 47-66.

864 Morad, S., Ketzer, J.M., DeRos, F., 2000. Spatial and temporal distribution of diagenetic
alterations in siliciclastic rocks: implication for mass transfer in sedimentary basins.

866 *Sedimentology*, 47, 95–120.

- 868 Morley, C.K., 2012. Late Cretaceous-Early Palaeogene tectonic development of SE Asia.
Earth Sci. Rev., 115, 37–75.
- 870
- Morley, C.K., 2013. Discussion of tectonic models for Cenozoic strike-slip fault-affected
872 continental margins of mainland SE Asia. *J. Asian Earth Sci.*, 76, 137–151.
- 874 Mullins, H.T., Wise, S.W., Land, L.S., Siegel, D.I., Masters, P.M., Edward, J., Price, K.R.,
1985. Geology Authigenic dolomite in Bahamian peri-platform slope sediment. *Geology*, 13,
876 4, 292–295.
- 878 Park, R.K., Matter, A., Tonkin, P.C., 1995. Porosity evolution in the Batu Raja carbonates of
the Sunda Basin Windows of opportunity. Indonesian Petroleum Association, 24th Annual
880 Convention. pp. 63–184.
- 882 Paumard, V., Zuckmeyer, E., Boichard, R., Jorry, S.J., Bourget, J., Borgomano, J., Maurin,
T., Ferry, J.N., 2017. Evolution of Late Oligocene - Early Miocene attached and isolated
884 carbonate platforms in a volcanic ridge context (Maldives type), Yadana field, offshore
Myanmar. *Mar. Petrol. Geol.*, 81, 361–387.
- 886
- Pingitore, N.E., 1976. Vadose and Phreatic Diagenesis: Processes, Products and their
888 Recognition in Corals. *J. Sediment.Res.*, 46, 985–1006.

- 890 Rabier, C., Anguy, Y., Cabioch, G., Genthon, P., 2008. Characterization of various stages of
calcitization in *Porites* sp corals from uplifted reefs - Case studies from New Caledonia,
892 Vanuatu, and Futuna (South-West Pacific). *Sediment. Geol.*, 211, 73–86.
- 894 Racey, A. and Ridd, M.F., 2015. Petroleum geology of the Moattama Region, Myanmar, in:
Racey, A and Ridd, M.F. (Eds.), *Petroleum Geology of Myanmar*, Geol. Soc. Memoir 45, pp.
896 63-81.
- 898 Raju, D.V.R., Gouveia, A.D, Murty, C.S., 1981. Some physical characteristics of Andaman
Sea waters during winter. *Indian J. Mar. Sc.*, 10, 211-218.
- 900
- Reaves, C.M., 1986. Organic matter metabolizability and calcium carbonate dissolution in
902 nearshore marine muds. *J. Sediment. Res.*, 56, 4, pp. 486–494.
- 904 Richard, J., Sizun, J.P., Machhour, L. 2007. Development and compartmentalization of
chalky carbonate reservoirs: the Urgonian Jura-Bas Dauphiné platform model (Génissiat,
906 southeastern France). *Sediment. Geol.*, 198, 195–207.
- 908 Saller, A.H., 1984. Petrologic and geochemical constraints on the origin of subsurface
dolomite, Enewetak Atoll: an example of dolomitization by normal seawater. *Geology*, 12,
910 217–220.

- 912 Saller, A.H., Moore, C.H., 1989. Meteoric diagenesis, marine diagenesis, and microporosity
in Pleistocene and Oligocene limestones, Enewetak Atoll, Marshall Islands. *Sediment. Geol.*,
914 63, 253–272.
- 916 Saller, A.H., Vijaya, S., 2002. Depositional and diagenetic history of the Kerendan carbonate
platform, Oligocene, Central Kalimantan, Indonesia. *J. Pet. Geol.* 25, 123–150.
- 918
- Sanders, D., 2003. Syndepositional dissolution of calcium carbonate in neritic carbonate
920 environments: Geological recognition, processes, potential significance. *J. African Earth Sci.*,
36, 99-134.
- 922
- Sattler, U., Zampetti, V., Schlager, W., Immenhauser, A., 2004. Late leaching under deep
924 burial conditions: A case study from the Miocene Zhujiang Carbonate Reservoir, South China
Sea. *Mar. Petrol. Geol.*, 21, 977–992.
- 926
- Sun, Q. S., Esteban, M., 1994. Paleoclimatic Controls on Sedimentation, Diagenesis, and
928 Reservoir Quality- Lessons from Miocene Carbonates. *AAPG Bull.*, 78, 519–543.
- 930 Suzuki, Y., Iryu, Y., Inagaki, S., Yamada, T., Aizawa, S., Budd, D.A., 2006. Origin of atoll
dolomites distinguished by geochemistry and crystal chemistry: Kita-daito-jima, northern
932 Philippine Sea. *Sediment. Geol.*, 183, 181–202.

- 934 Swart, P.K., 2015. The geochemistry of carbonate diagenesis: The past, present and future. *Sedimentology*, 62, 1233–1304.
- 936
- Takayanagi, H., Iryu, Y., Yamada, T., Oda, M., Yamamoto, K., Sato, T., Chiyonobu, S.,
938 Nishimura, A., Nakazawa, T., Shiokawa, S., 2007. Carbonate deposits on submerged
seamounts in the northwestern Pacific Ocean. *Isl. Arc*, 16, 394–419.
- 940
- Vahrenkamp, V.C., 1998. Miocene carbonates of the Luconia province, offshore Sarawak:
942 implications for regional geology and reservoir properties from Strontium-isotope
stratigraphy. *Geol. Soc. Malaysia Bull.*, 42, 1–13.
- 944
- Vahrenkamp, V.C., David, F., Duijndam, P., Newall, M., Crevello, P., 2004. Growth
946 architecture, faulting, and karstification of a middle Miocene carbonate platform, Luconia
Province, offshore Sarawak, Malaysia, in: Eberli, G.P., Masferro, J.L. and “Rick” Sarg, J. F.
948 (Eds.), *Seismic Imaging of Carbonate Reservoirs and Systems*, AAPG Memoir 81, pp. 329–
350.
- 950 Veizer, J., 1983. Chemical diagenesis of carbonates: theory and application of trace element
technique. In: Arthur, M.A., Anderson, T. F., Kaplan, I. R., Veizer, J., Land, L.S. (Eds.),
952 *Stable Isotopes in Sedimentary Geology*, SEPM Short Course Notes, 10, pp. 1–100.
- 954 Volery, C., Davaud, E., Foubert, A., Caline, B., 2010. Lacustrine microporous micrites of the
Madrid Basin (Late Miocene, Spain) as analogues for shallow-marine carbonates of the

956 Mishrif reservoir formation (Cenomanian to Early Turonian, Middle East). *Facies*, 56, 385–
397.

958

Warrlich, G., Taberner, C., Wenche, A., Stephenson, B., Esteban, M., Boya-Ferrero, M.,
960 Dombrowski, A., van Konijnenburg, J.H., 2010. The Impact of Post-depositional Processes
on Reservoir Properties: Two Case Studies of Tertiary Carbonate Buildup Gas Fields in
962 Southeast Asia (Malampaya and E11), in: Morgan, W.A., George, A.D., Harris, P.M.,
Kupecz, J.A., Sarg, J.F. (Eds.), *Cenozoic Carbonates Systems of Australasia*, SEPM Special
964 Publication 95, pp. 99-128.

966 Webb, G.E., Nothdurft, L.D., Kamber, B.S., Kloprogge, J.T., Zhao, J.X., 2009. Rare earth
element geochemistry of scleractinian coral skeleton during meteoric diagenesis: A sequence
968 through neomorphism of aragonite to calcite. *Sedimentology*, 56, 1433–1463.

970 Wilson, M.E.J., 2008. Global and regional influences on equatorial shallow-marine
carbonates during the Cenozoic. *Palaeog. Palaeocl. Palaeoec.*, 265, 262–274.

972

Wilson, M.E.J., Hall, R., 2010. Tectonic influences on SE Asian carbonate systems and their
974 reservoir development, in: Morgan, W.A., George, A.D., Harris, P.M., Kupecz, J.A., Sarg,
J.F. (Eds.), *Cenozoic Carbonates Systems of Australasia*, SEPM Special Publication 95, pp.
976 13-40.

978 Zachos, J., Pagani, M., Sloan, L., Thomas, E., Billups, K., 2001. Trends, Rhythms, and
Aberrations in Global Climate 65 Ma to Present. *Science*, 292, 686–693.

980

Zampetti, V., 2010, Controlling factors of a Miocene carbonate platform: Implications for
982 platform architecture and offplatform reservoirs (Luconia province, Malaysia), in: Morgan,
W.A., George, A.D., Harris, P.M., Kupecz, J.A., Sarg, J.F. (Eds.), *Cenozoic Carbonates*
984 *Systems of Australasia*, SEPM Special Publication 95, pp. 126–146.

986 Zampetti, V., Schlager, W., van Konijnenburg, J.H., Everts, A.J., 2004. Architecture and
growth history of a Miocene carbonate platform from 3D seismic reflection data; Luconia
988 province, offshore Sarawak, Malaysia. *Mar. Petrol. Geol.*, 21, 517–534.

990

Zampetti, V., Sattler, U., Braaksma, H., 2005. Well log and seismic character of Liuhua 11-1
992 Field, South China Sea; relationship between diagenesis and seismic reflections. *Sedimentary*
Geology, 175, 217–236

994

996 **Figure captions**

998 Fig. 1. Geographical and geological setting of the Yadana gas field: (A) Geographical and
tectonic settings of the Andaman Sea and the Yadana Field (after Curray, 2005); (B) Depth
1000 map of top reservoir and well location. (C) Interpreted regional 2D seismic profile (two-way-
time) through the Yadana high (see location on A). (D) Interpreted seismic profile (depth) of
1002 the Yadana field crossing the wells WELL-4 and WELL-2, showing the lithostratigraphic
units and the gaswater contact (yellow dotted line) (see location on A). (E). Lithostratigraphic
1004 column of the Yadana platform.

1006 Fig. 2. Well-correlations and stratigraphic architecture of the Yadana platform, based on large
benthic foraminiferal biostratigraphy, well-to seismic tie (vertical resolution ~10 m) and
1008 correlation of key stratigraphic surfaces. Key seismic reflectors (H9, H9A, H9B) are
positioned on the well-correlation panel.

1010

Fig.3. Microphotographs of lithofacies from the Upper Burman Limestone. (A) WELL-1
1012 1284.15 mCD: Coralline algal rudstone (LF1). (B) WELL-1 1319.04 mCD: Large benthic
foraminiferal rudstone (LF2.1). (C) WELL-2 1324.78 mCD: Large benthic foraminiferal
1014 floatstone (LF2.2). (D) WELL-1 1325.96 mCD: Coral floatstone (LF3) with curved fractures
(arrow) indicating incipient brecciation.

1016

Fig.4. Microphotographs of selected diagenetic features from the Upper Burman Limestone.
1018 (A, B): WELL-2 1355.6 mCD: Isopacheous rim cement C1 and blocky calcite cement C2

under under polarized-light microscopy (A) and cathodoluminescence (B); Three zones are
1020 distinguished from cathodoluminescence: (1) C1 rim cement, lining the pore space, non-
luminescent, (2) early phase of C2 cement formed by concentric, thin (20 μ m) bands with dull
1022 to bright luminescence and (3) later, non-luminescent, C2 cement (diagenetic facies: G-DF2).
(C) WELL-3 1319.49 mCD: Isopacheous C1 rim cement and blocky calcite cement C2
1024 infilling the intergranular pore space of a foraminiferal rudstone (diagenetic facies: G-DF2). A
syntaxial calcite cement (*Syn*) develops around an echinoderm (*Ech*) fragment. (D) WELL-1
1026 1328.03 mCD: equigranular sparry calcite replacing a coral fragment (C2'). (E) WELL-4
1326.45 mCD: Fragment of calcitized coral (CX) set in a micrite mud sediment which
1028 postdates the development of CX calcite overgrowths (red arrows) around the coral. (F)
WELL-4 1337.7 mCD: core picture showing brownish calcitized coral (CX) within a
1030 brecciated interval (diagenetic facies: G-DF3).

1032 Fig 5. Micrite microfabrics identified under SEM: (A) Highly porous calcimicrite
microtexture M1 showing loosely-packed, dominantly anhedral, subrounded micrite particles.
1034 Such micrites display commonly microvugs (diameter: 5-10 μ) and relatively minor particle
coalescence (gas zone). Few micrite particles exhibit subhedral morphology (arrow), (B)
1036 Highly porous calcimicrite microtexture M1, mixed with larger euhedral dolomicrosparite
crystals (dol) (gas zone) (C) Low porosity calcimicrite microtexture M2 showing densely-
1038 packed, strongly coalescent, anhedral micrite particles (gas zone). (D) Low porosity micrite
microtexture M3 showing densely-packed, subhedral to euhedral calcimicrite crystals (water
1040 zone) (E) Low porosity micrite microtexture M3 showing densely-packed, euhedral
calcimicrite crystals encasing smaller, rounded micrite particles (arrow) (water zone). (D)
1042 Euhedral dolomicrite (M4) replacing a coralline algae (gas zone).

1044 Fig.6. Micro-photographs of early marine dissolution features from the Upper Burman
Limestone under polarized light microscopy: (A) WELL-3 1311.84 mCD: Coral floatstone
1046 whose scleractinian elements have been dissolved; the resulting moldic pores are infilled with
a bioclastic micrite (BM) which is similar in nature to that of the floatstone matrix thus
1048 leading to a faint-ghost fabric (diagenetic facies: G-DF4). (B) Close up on dissolved coral
calyces infilled by bioclastic mud lime (BM). (C) WELL-1 1256.6 mCD. Core sample
1050 showing a highly microporous, brecciated coral floatstone (LF3) with irregular-shaped clasts
showing deep embayments (white arrows) (diagenetic facies: G-DF4).

1052

Fig.7. (A) WELL-3 1319.92 mCD: microphotograph of moldic pores and vugs within a
1054 foraminiferal grainstone. The intergranular pore space is entirely occluded by C2 sparry
calcite (diagenetic facies: G-DF2) (C2). (B) WELL-4 1286 mCD: microphotograph of a
1056 foraminiferal packstone-floatstone whose matrix is partially replaced by dolomicrosparite (not
stained by alizarine) (diagenetic facies: G-DF1C); (C) WELL-3 1308.05 mCD: core
1058 photograph of a hardground surface, at the top of a carbonate breccia composed of poorly
displaced, tight elements of coral-rich and echinodermal floatstone (LF3) (diagenetic facies:
1060 G-DF4). The hardground is sharply overlain by highly microporous, coralline algal-
foraminiferal floatstone (diagenetic facies: G-DF1A). The inter-clast space of the hardground
1062 breccia is filled by the overlying microporous sediment. (D) WELL-2: 1354.56m CD:
foraminiferal grainstone-rudstone from the water zone (diagenetic facies: W-DF1). The
1064 relatively low porosity (14%) of the sample is related to the lack of intergranular and
moldic/vuggy macroporosity and to the microporosity reduction by calcite micro-overgrowth
1066 development within micritized bioclasts. (E) WELL-2 1284.56 mCD: microphotograph of a

coralline algal-foraminiferal floatstone showing a stylolite (red line) which is overprinted by a
1068 dissolution vug (diagenetic facies: G-DF1A). (F) WELL-4 1347.14: Echinodermal floatstone
showing pervasive moldic and vuggy porosity (G-DF1B). (G) Close up of (E) showing
1070 dissolution features affecting a stylolite (arrows).

1072 Fig.8. WELL-2, (A) cored interval: lithofacies, depositional textures, carbon and oxygen
isotope ratios, porosity (laboratory measurements on plugs), water saturation, pore type
1074 distribution (after image analysis of thin-sections), diagenetic features and diagenetic facies.
(B) Vertical variations of porosity within the Upper Burman Limestone, from well logs (dark
1076 curve) and smoothed values (moving average over a 2 meter-thick interval: red curve),
showing the decrease in average porosity below the gas-water contact.

1078

Fig.9. Carbon and oxygen isotopic signatures of the Upper Burman Limestone (A) $\delta^{18}\text{O}$ - $\delta^{13}\text{C}$
1080 plot for selected bioclasts (large benthic foraminifera, coralline algae and calcitized corals)
and bulk-rock measurements (grey dots) in the background (B) $\delta^{18}\text{O}$ - $\delta^{13}\text{C}$ plot for the 3
1082 calcimicrite microfabrics identified in the Upper Burman Limestone, and bulk-rock
measurements (grey dots) in the background (C) $\delta^{18}\text{O}$ - $\delta^{13}\text{C}$ plot for calcite cements, dolomite,
1084 as well as for carbonate breccia clasts and matrix; bulk-rock measurements (grey dots) are
plotted in the background (D, E) $\delta^{18}\text{O}$ - $\delta^{13}\text{C}$ plots for bulk-rock measurements: samples are
1086 labeled according to the diagenetic facies within the gas zone (D) and water zone (E).

1088 Fig. 10. WELL-1, -3 and -4, cored interval: lithofacies, depositional textures, carbon and
oxygen isotope ratios, porosity (laboratory measurements on plugs), water saturation,
1090 dolomite and dissolution vug occurrence and diagenetic facies.

1092 Fig.11. Diagenetic facies zonation of the four studied wells, vertical variations of plug
porosity and remarkable surfaces (hardgrounds and potential subaerial surface).

1094

Fig.12. Paragenesis and porosity evolution of the Upper Burman Limestone and subsidence
1096 curve.

1098 **Table captions**

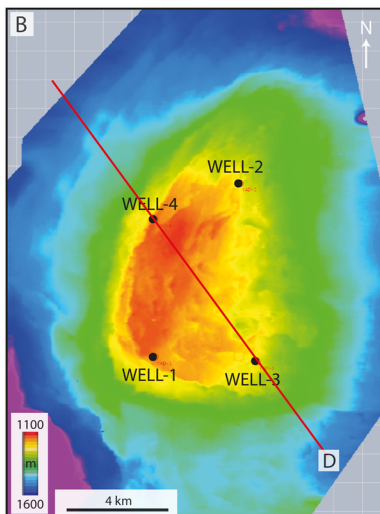
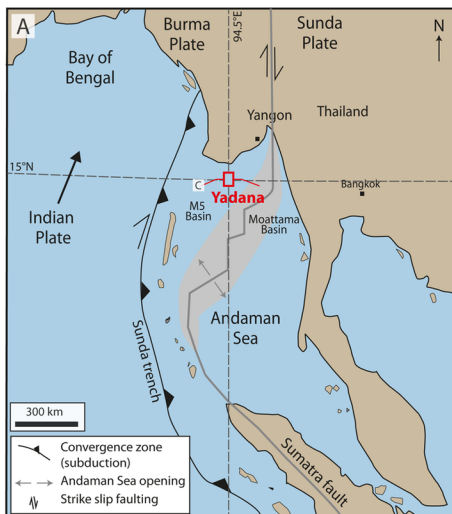
1100 **Table 1:** depositional lithofacies and skeletal components of the Upper Burma Limestone

1102 **Table 2:** Definition and properties of the diagenetic facies from the Upper Burman Limestone

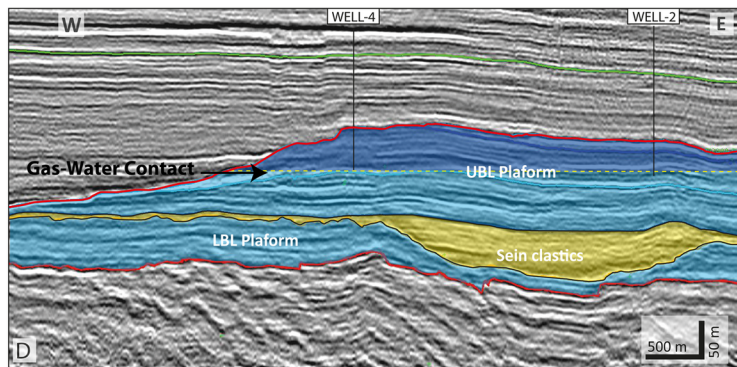
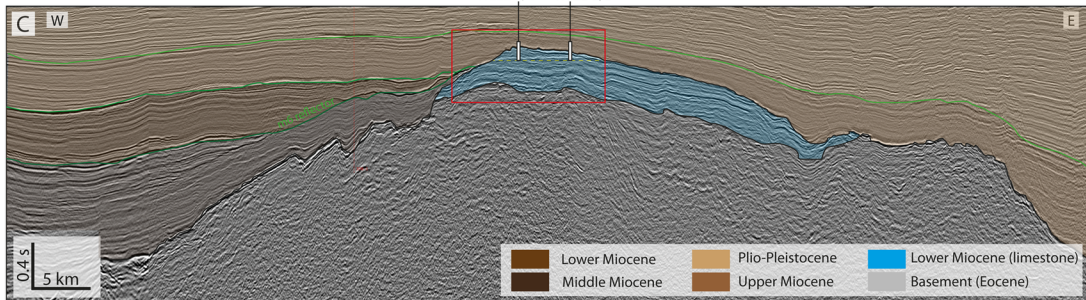
1104 **Table 2:** Concentrations of selected major and trace elements on bulk rock samples and various carbonate components

1106

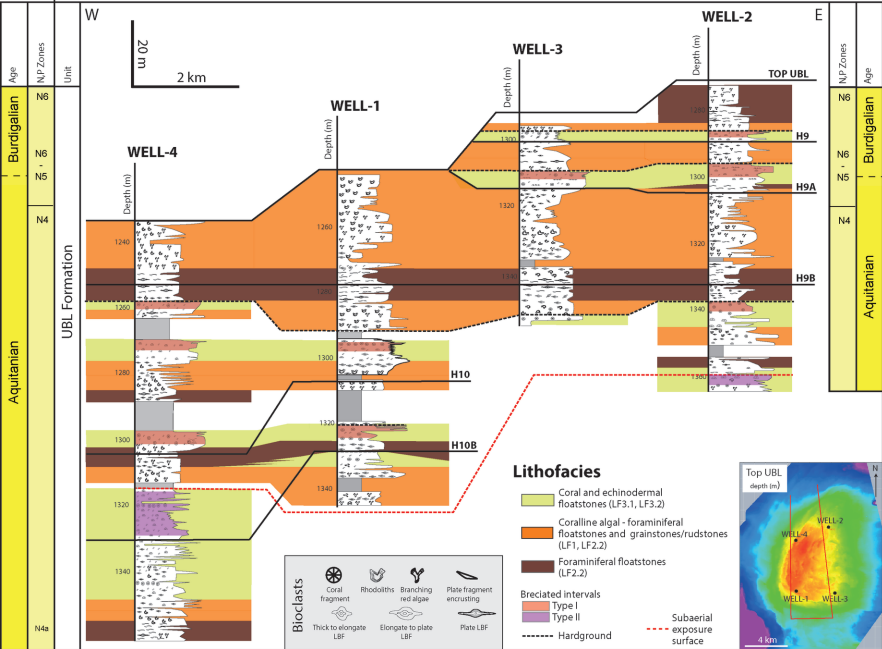
1108

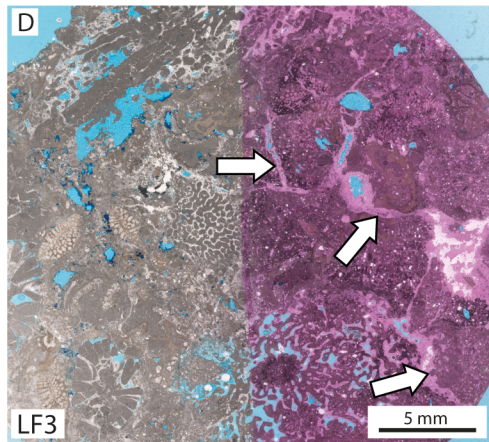
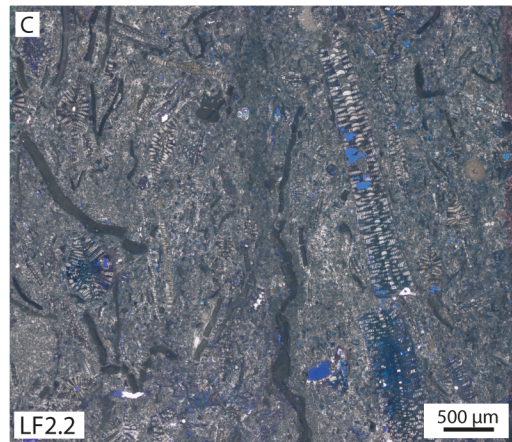
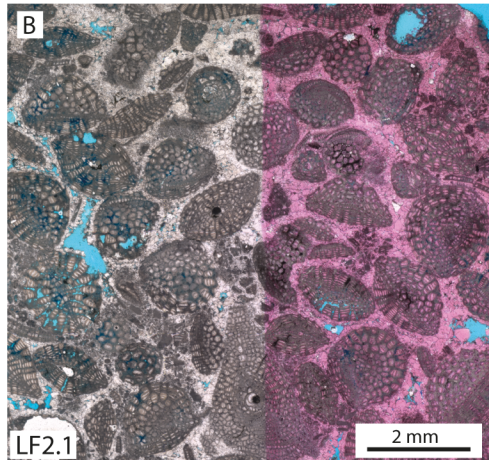
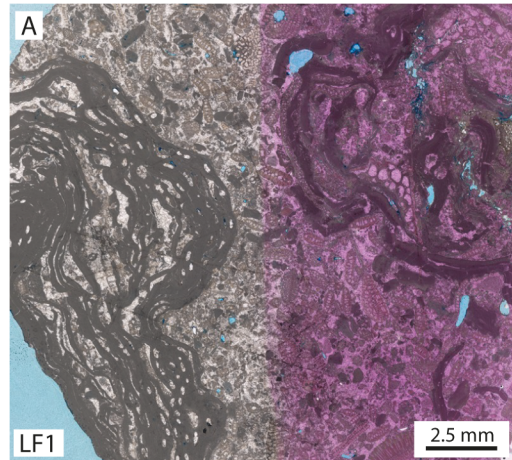


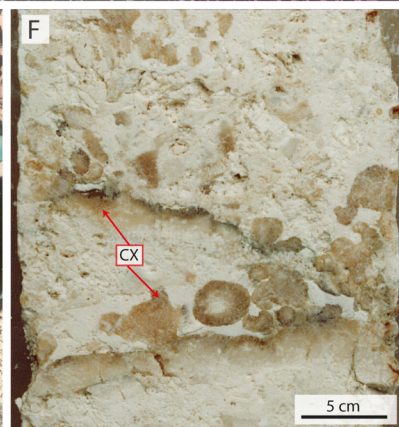
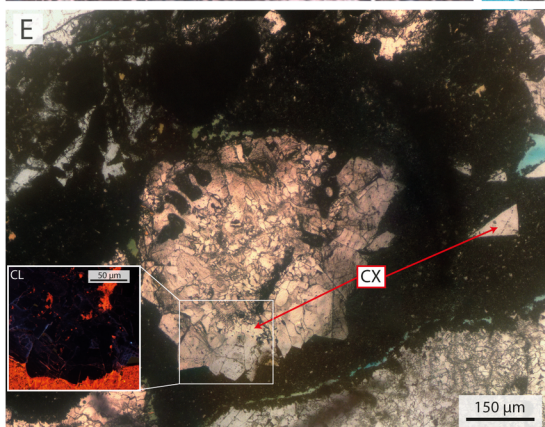
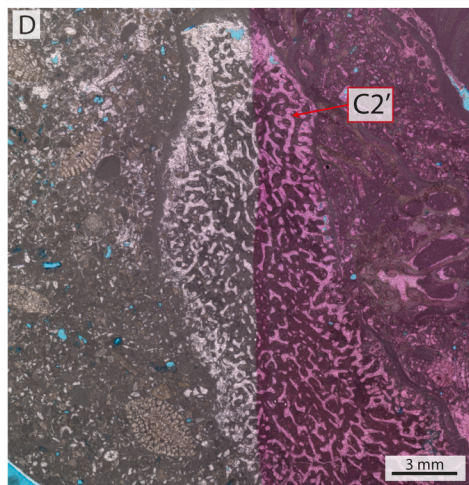
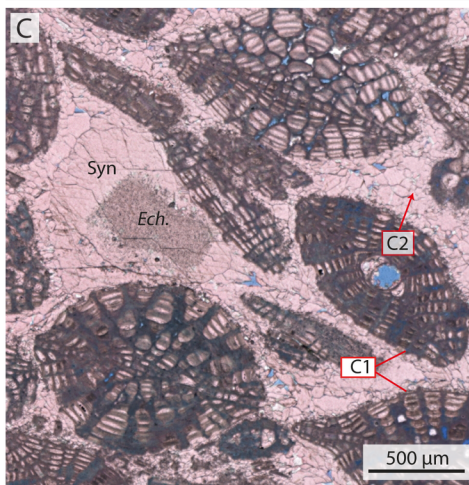
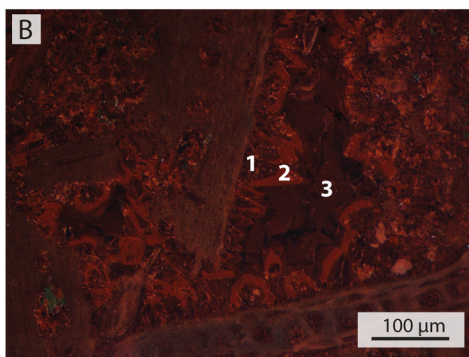
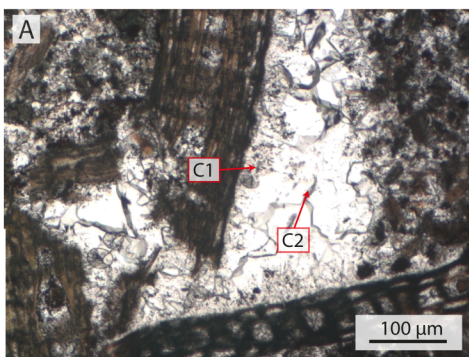
M5 Basin Yadana High Volcano high (3CA) Moattama Basin



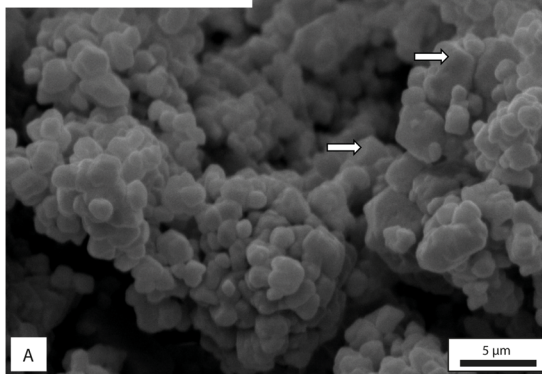
Depth (m)	Lithological column	Formation	Age
0 - 1000	IRRAWADDY Fluvio / deltaic sandstone, claystone	IRRAWADDY Fluvio / deltaic sandstone, claystone	LOWER PLIOCENE
1000 - 1200	BADAMYAR Prodelta Sands	BADAMYAR Prodelta Sands	Late MIOCENE
1200 - 1350	PYAWBWE Marine Shales	PYAWBWE Marine Shales	Late MIOCENE
1350 - 1500	UPPER BURMA limestone (UBL) carbonate platform	UPPER BURMA limestone (UBL) carbonate platform	Early MIOCENE
1500 - 1650	SEIN clastics	SEIN clastics	Late OLIGO
1650 - 1800	Lower BURMA Limestone (LBL) carbonate platform	Lower BURMA Limestone (LBL) carbonate platform	Early OLIGO-CENE
1800 - 2000	Volcanoclastic basement	Volcanoclastic basement	Eocene



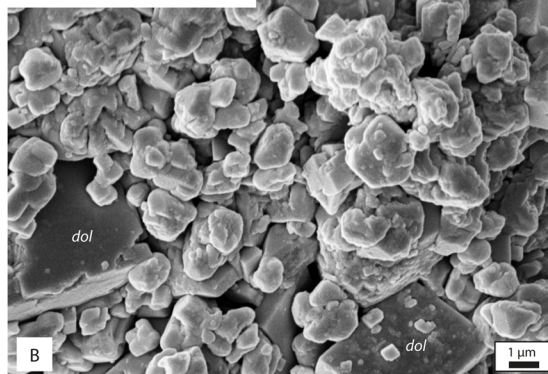




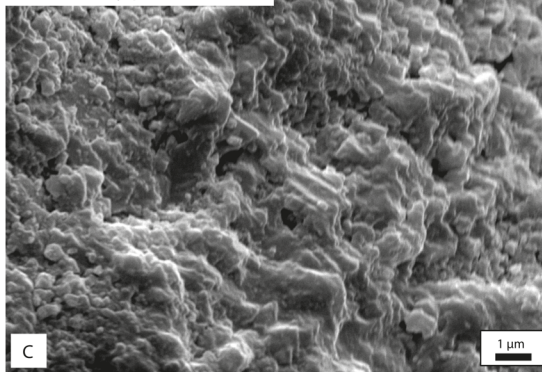
M1: subrounded micrite



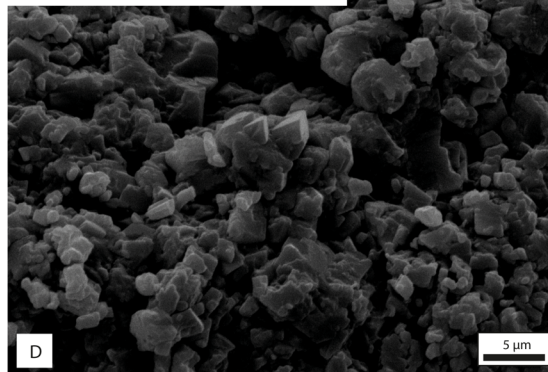
M1: subrounded micrite



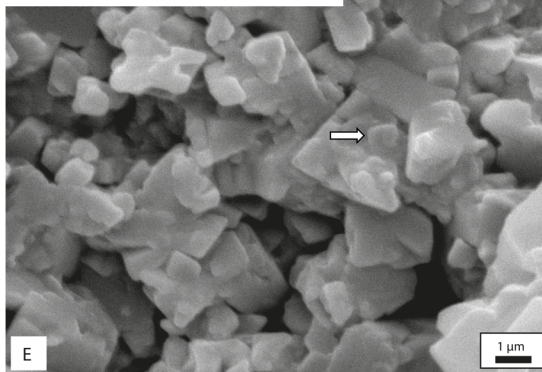
M2: densely packed micrite



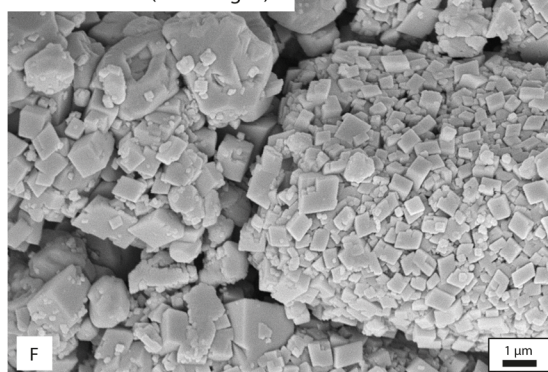
M3: subhedral to euhedral micrite

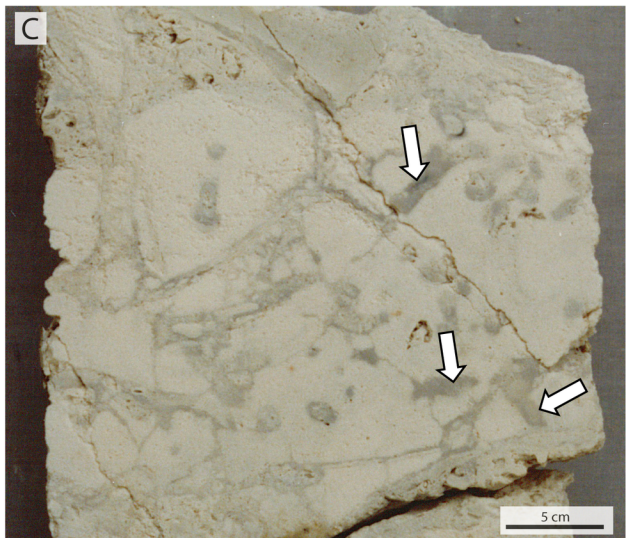
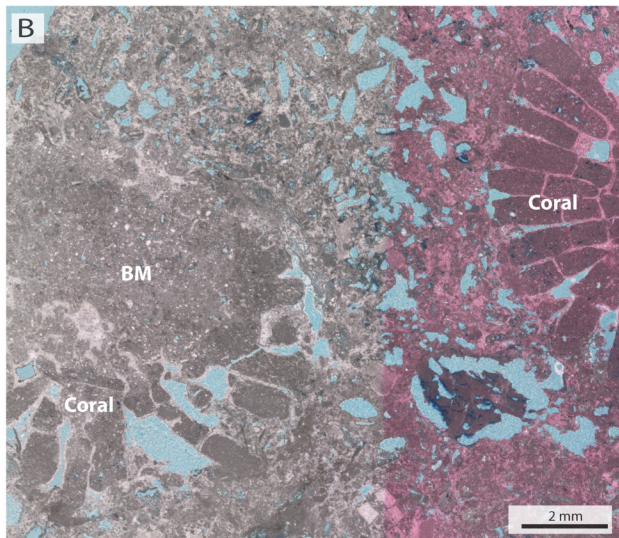
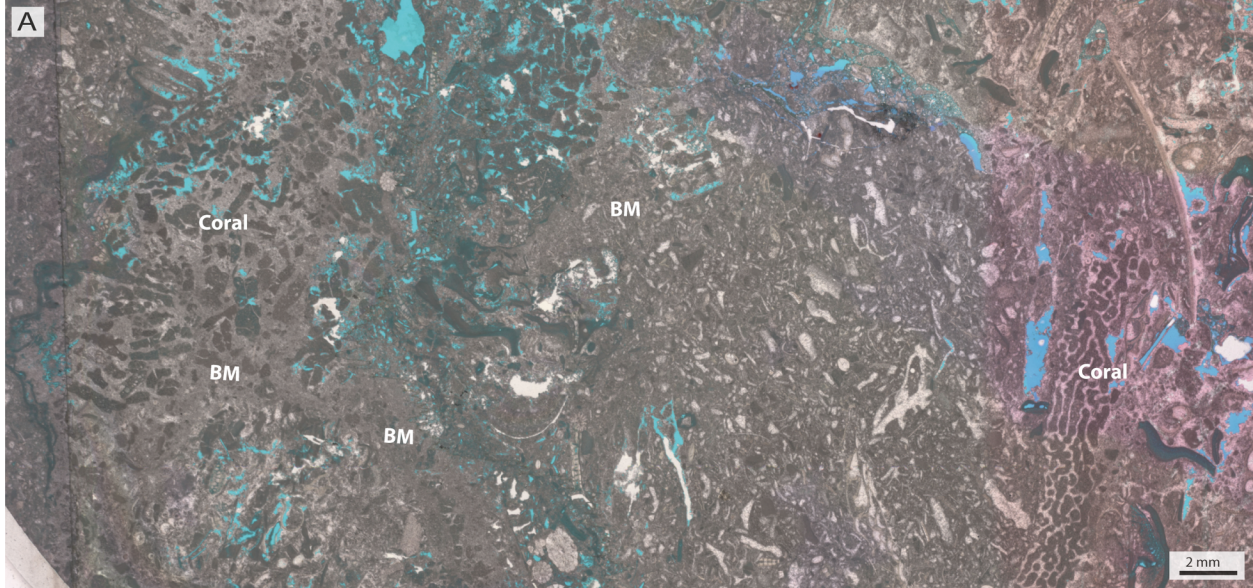


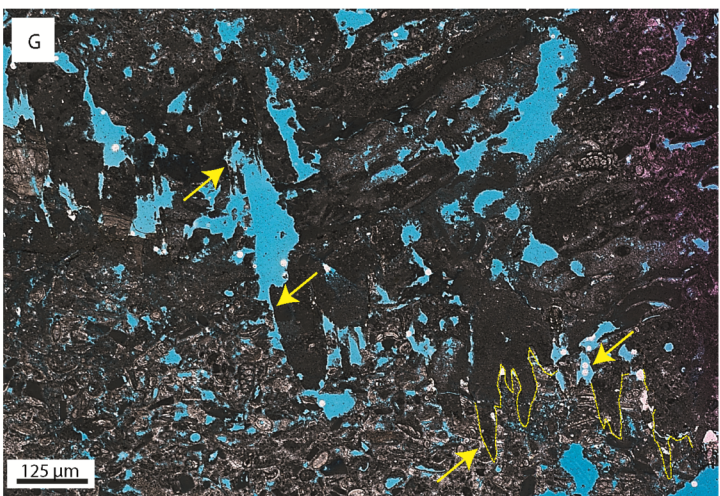
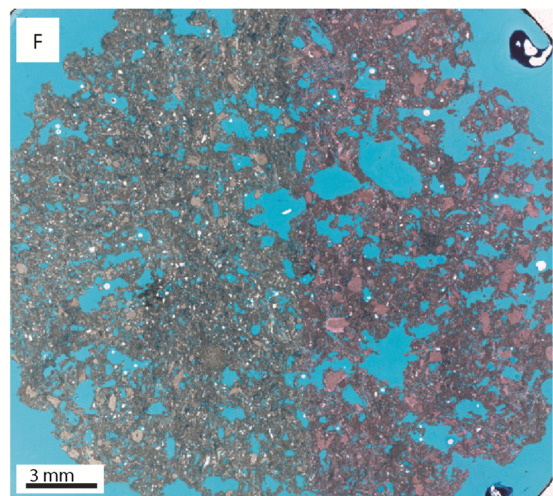
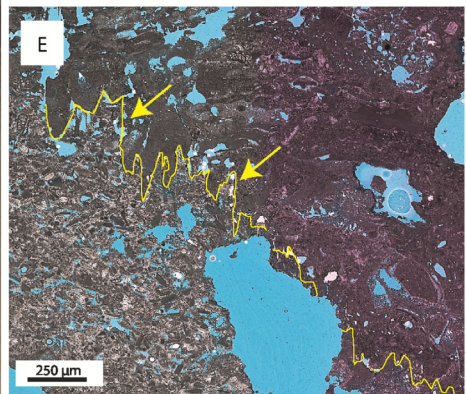
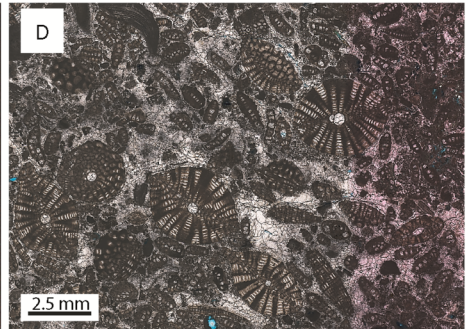
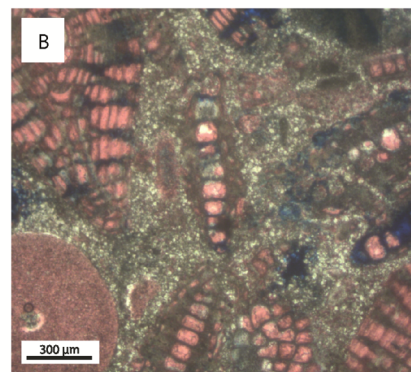
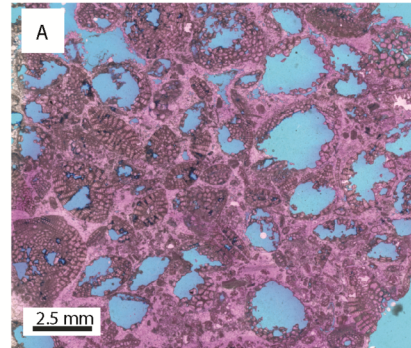
M3: subhedral to euhedral micrite

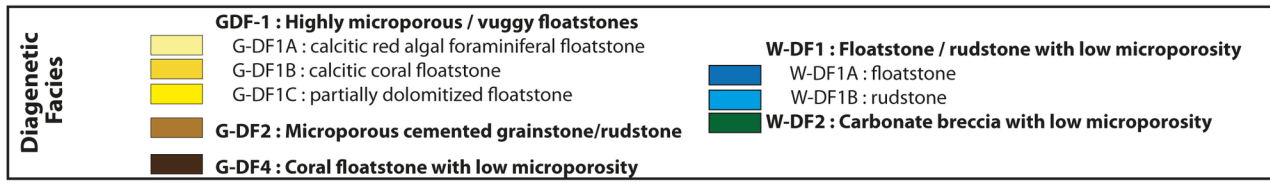
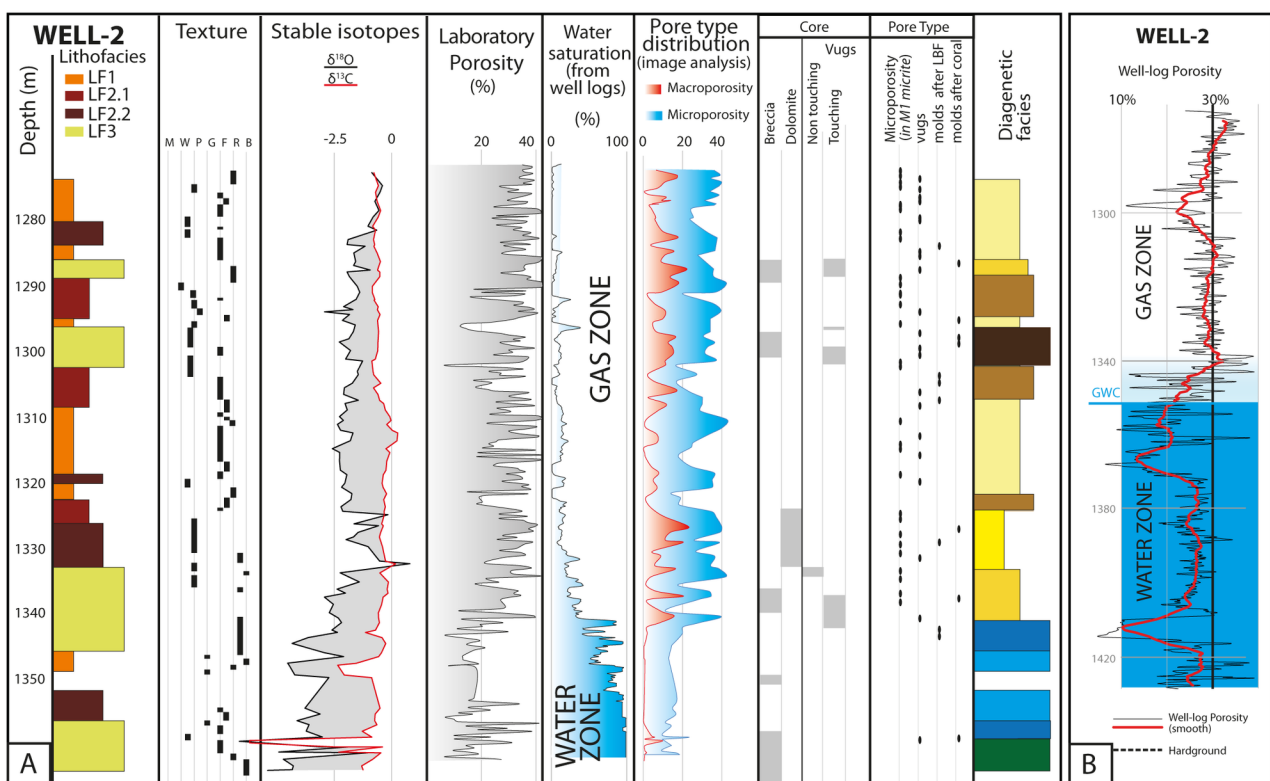


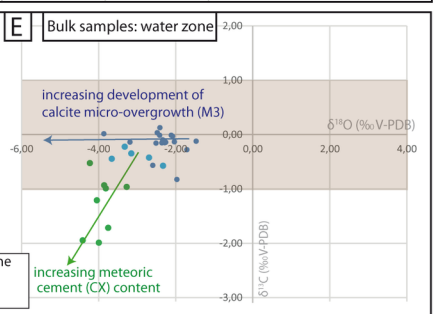
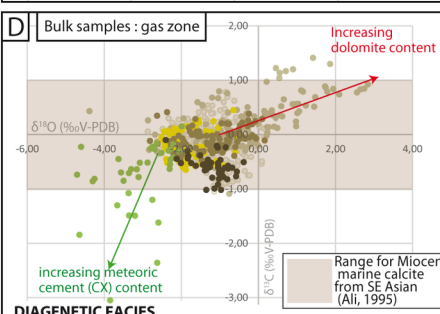
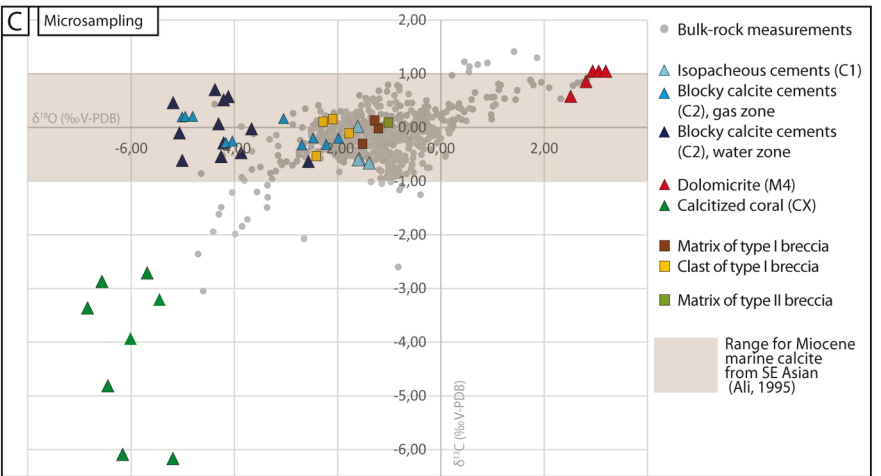
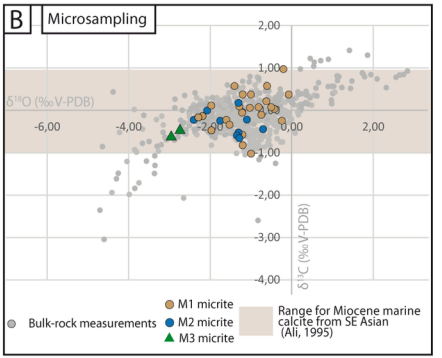
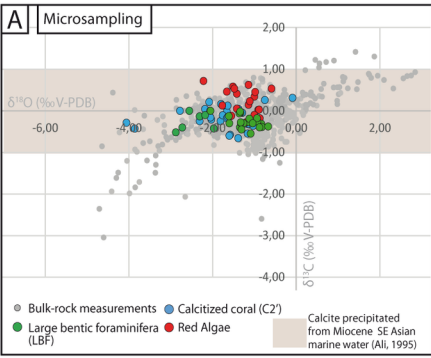
M4: dolomite (in red algae)











DIAGENETIC FACIES

GDF-1 Highly microporous and moldic/ugly, mud-supported carbonates

- A: calcitic red algal/foraminiferal floatstone
- B: calcitic coral floatstones
- C: dolomitic coral floatstones

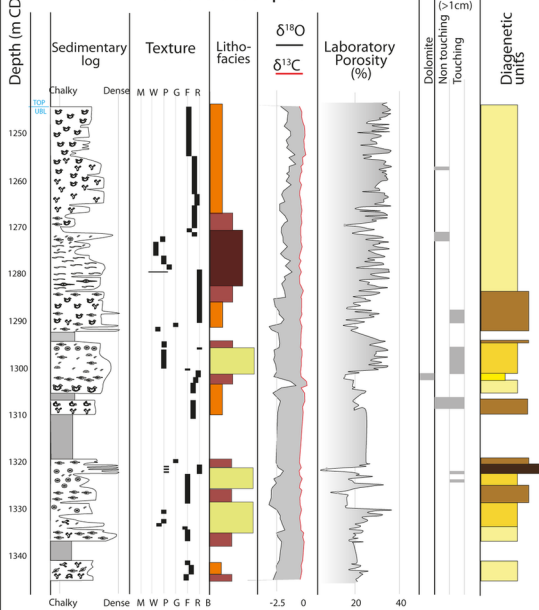
- GDF-2** Microporous cemented grainstones-rudstones
- GDF-3** Microporous and vuggy carbonate breccia
- GDF-4** Coral floatstones with low matrix microporosity

WDF-1 Floatstones and rudstones with low microporosity

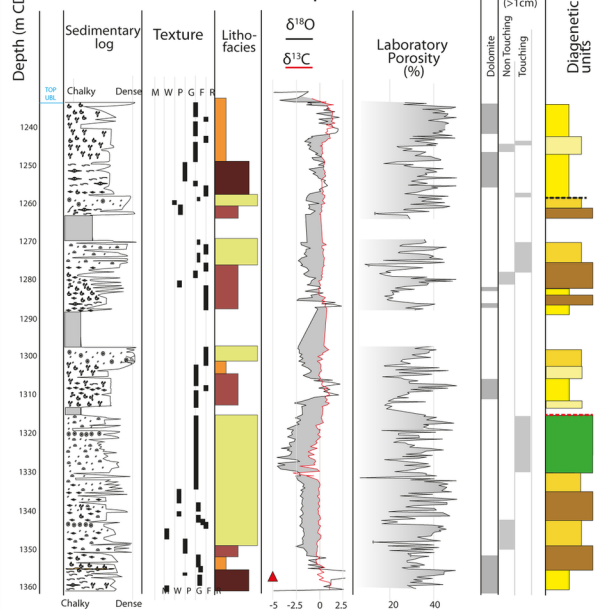
- A: Floatstones
- B: Rudstones

WDF-2 Carbonate breccia with low microporosity

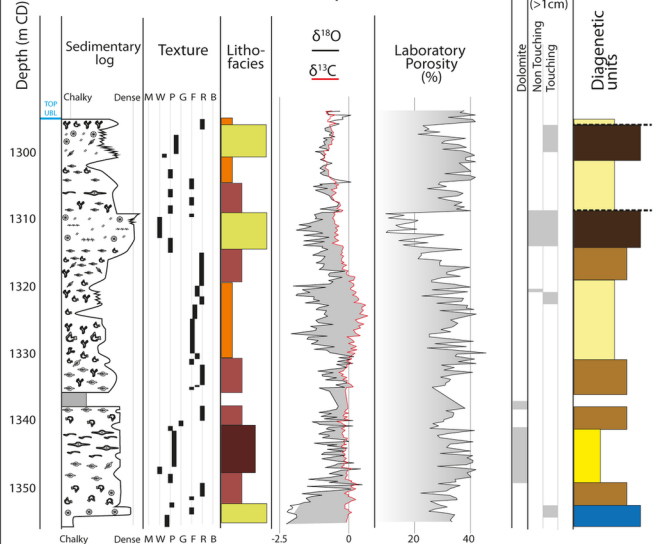
WELL-1 : Core description



WELL-4 : Core description



WELL-3 : Core description



Bioclasts

- Coral fragment
- Rhodoliths
- Branching red algae
- Plate fragment encrusting
- Thick to elongate LBF
- Elongate to plate LBF
- Plate LBF

Lithofacies

- LF1: Coralline algal - foraminiferal floatstone
- LF2.1: Large benthic foraminiferal rudstone
- LF2.2: Large benthic foraminiferal floatstone
- LF3: Coral floatstone

Diagenetic Facies

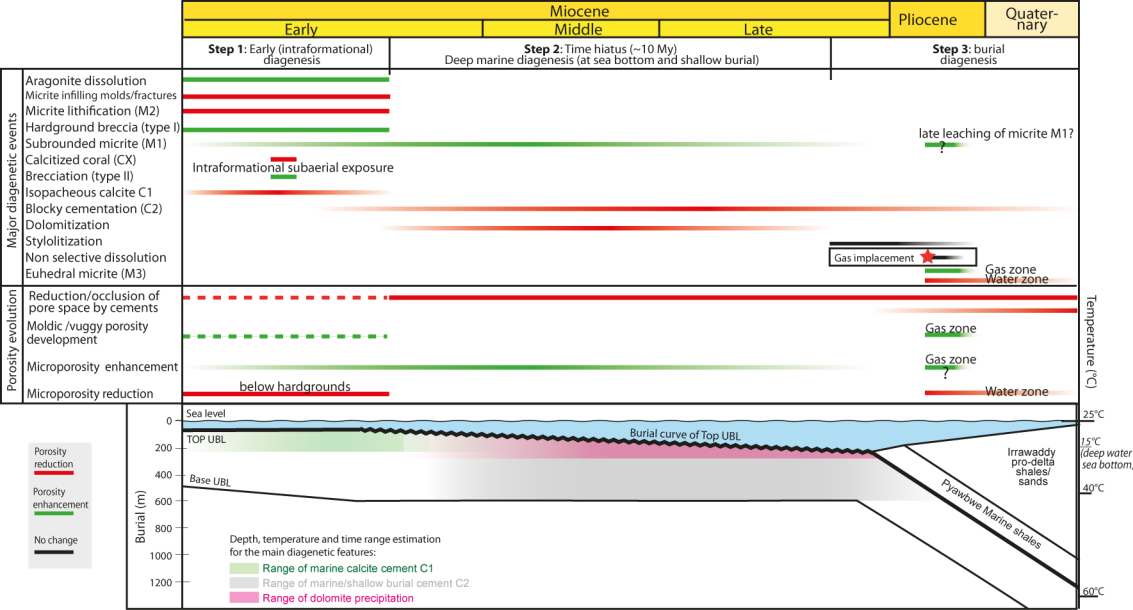
- GDF-1: Highly microporous / vuggy floatstones
 - G-DF1A: calcitic red algal foraminiferal floatstone
 - G-DF1B: calcitic coral floatstone
 - G-DF1C: partially dolomitized floatstone
- G-DF2: Microporous cemented grainstone/rudstone
- G-DF3: Microporous and vuggy carbonate breccia
- G-DF4: Coral floatstone with low microporosity

W-DF1: Floatstone / rudstone with low microporosity

- W-DF1A: floatstone
- W-DF1B: rudstone

W-DF2: Carbonate breccia with low microporosity

----- Hardground
- - - - - Subaerial exposure surface



Lithofacies	Skeletal components
LF1. Coralline algal floatstone to rudstone with a coralline algal-foraminiferal wackestone to packestone matrix.	Heterometric spheroidal-ellipsoidal rhodoliths (1-10 cm in diameter) or pieces of branching coralline algae (<i>Lithothamnion</i> , <i>Mesophyllum</i> and <i>Sporolithon</i>). The foraminiferal assemblage is dominated by <i>Spiroclypeus tidoenganensis</i> and <i>Nephrolepidina sumatrensis</i> , with common occurrences of <i>Miogypsinoidea</i> , <i>Miogypsina</i> and <i>Heterostegina (Vlerkina)</i>
LF2.1. Large benthic foraminiferal rudstone with common red algal fragments.	The foraminiferal assemblage is dominated by <i>Lepidocyclina (Nephrolepidina) sumatrensis</i> , <i>L. (N.) oneatensis</i> , and <i>Spiroclypeus tidoenganensis</i> with rarer specimens of <i>Amphistegina</i> , <i>Heterostegina</i> , <i>Miogypsina</i> , and <i>Miogypsinoidea</i> . Coralline algae mainly include branching and warty <i>Lithothamnion</i> , <i>Mesophyllum</i> and branching <i>Sporolithon</i> .
LF2.2. Large benthic floatstone with coralline algal wackestone / packestone matrix.	Large benthic foraminifera are large (up to 2cm), thin-shelled, commonly well preserved, and typically horizontally-oriented. Dominated by <i>Spiroclypeus tidoenganensis</i> with common occurrences of <i>Cycloclypeus</i> ... Laminar and loose <i>Mesophyllum</i> , together with branching <i>Lithothamnion</i> are common.
LF3.1 Coral floatstone with an echinodermal wackestone matrix. Coral dominated intervals are frequently brecciated at the top. Thin intervals of echinodermal wackestone with sparse corals may be interbedded within coral-echinodermal floatstones.	Scleractinian floatstone consists of transported fragile branches or massive fragments of <i>Faviids</i> and <i>Pocilloporids</i> . Ophiuroids, echinoids, small pieces of non-articulated coralline algae and occasional broken <i>Spiroclypeus</i> and <i>lepidocyclinids</i> . Brecciated at the top units, elements are gravel to pebble-sized (typically 0.5-5 cm), angular, para-autochthonous. The inter-intraclast space is filled with a micrite containing various proportions of small echinoderm fragments.
LF3.2. Echinodermal wackestone Commonly brecciated, like LF3.1	Bioclastic wackestone is dominated by echinoderm pieces including ophiuroid ossicles and echinoids, small size fragments of coralline algae. Frequently interbedded between coral floatstone LF3.1.

Table 1: depositional lithofacies and skeletal components of the Upper Burma Limestone

Diagenetic facies		Diagenetic features	Micrite micro-fabrics	Typical porosity range	Pore type association	$\delta^{13}\text{C}$ bulk signature (‰ PDB)	$\delta^{18}\text{O}$ bulk signature (‰ PDB)	Occurrence	Illustration
G-DF1	Highly microporous and moldic/vuggy, mud-supported carbonates	A: calcitic red algal and foraminiferal floatstones	M1	25-45%	High microporosity, high moldic and vuggy porosity	-1 to +1	-3 to 0		Fig.7 A, E
		B: calcitic coral floatstones	M1	25-45%	High microporosity, high moldic and vuggy porosity	-1 to +1	-3 to 0	Gas zone	Fig. 4 D
		C: partially dolomitized floatstones	M1 / M4	25-45%	High microporosity, high moldic and vuggy porosity	-0,5 to +1,5	-0,5 to +3		Fig.7 B
G-DF2	Microporous cemented grainstones-rudstones	Isopacheous calcite cement (C1) and blocky calcite cement (C2).	M1	18-30%	High microporosity, moldic porosity; rarer intergranular porosity	-0,5 to +0,5	-3 to 0	Gas zone	Fig.4 A, B, C
G-DF3	Microporous and vuggy carbonate breccia	Brecciation features (type II); neomorphosed corals into CX calcite; blocky calcite cement (C2); micritized bioclasts; leached bioclasts (corals, red algae and foraminifers) and matrix	M1	25-40%	High microporosity, inter-breccia clast porosity; moldic and vuggy porosity; rarer intergranular porosity	-3,5 to 0	-5 to -2	Gas zone	Fig. 4 E,F
G-DF4	Coral floatstones with low matrix microporosity	Brecciation features (type I); leached corals and micrite infills within molds (faint-ghost texture); leached bioclasts (corals, red algae and foraminifers)	M2	10-20%	Low microporosity; moldic to vuggy porosity	-1 to 0	-2 to 0	Gas zone	Fig.6 A, B, C; Fig. 7 C

W-DF1	Floatstones and rudstones with low intragranular and matrix microporosity	Micritized bioclasts; isopacheous calcite cement (C1) blocky calcite cement (C2); leached bioclasts (red algae and foraminifers) and matrix	M3	10-25%	Low microporosity; moldic to vuggy porosity	-1 to 0	-4 to -1,5	Water zone	Fig. 7 D
W-DF2	Carbonate breccia with low microporosity	Brecciation features (type II); neomorphosed corals into CX calcite; blocky calcite cement (C2); micritized bioclasts; leached bioclasts (corals, red algae and foraminifers) and matrix	M3	10-30%	Low microporosity; inter-breccia clast porosity; moldic to vuggy porosity	-2 to -0,5	-5 to -3	Water zone	

Table 2: Definition and properties of the diagenetic facies from the Upper Burman Limestone

Well	Sample depth (m)	Nature of the sample Detection limit	Mn ppm 5	Fe % 0.01	Mg % 0.01	Sr ppm 2	Ba ppm 1	Na % 0.01
WELL-1	1273.50	Large benthic foram.	128	0.03	1.94	551	90	0.22
WELL-1	1257.50	Coralline algae	31	0.03	1.38	486	31	0.13
WELL-1	1343.60	Coralline algae	24	0.02	0.48	574	1225	0.09
WELL-1	1249.00	Coralline algae	41	0.01	0.71	458	35	0.12
WELL-2	1277.50	Coralline algae	25	<0.01	0.9	407	76	0.15
WELL-2	1314.30	Coralline algae	18	<0.01	0.8	530	583	0.09
WELL-2	1319.16	Microporous matrix	35	0.03	1.19	450	16	0.09
WELL-2	1357.66	C2 calcite	17	<0.01	0.22	613	6	0.01
WELL-4	1326.50	CX calcite	11	<0.01	0.1	644	12	0.04
WELL-2	1362.40	CX calcite	<5	<0.01	0.14	2019	17	0.04
WELL-3	1298.36	bulk rock	69	0.01	0.16	360	27	0.03
WELL-3	1308.89	bulk rock	103	0.02	0.17	514	954	0.01
WELL-3	1309.00	bulk rock	34	0.01	0.21	528	2171	0.09
WELL-3	1311.00	bulk rock	100	0.04	0.15	422	55	0.02
WELL-2	1289.96	bulk rock	157	0.02	0.17	465	2850	0.04
WELL-4	1270.82	bulk rock	55	<0.01	0.22	536	10	0.13
WELL-4	1232.50	bulk rock (TOP UBL)	356	0.66	0.82	663	178	0.09

Table 3: Concentrations of selected major and trace elements on bulk rock samples and various carbonate components